Geophysical characterisation of active thermogenic oil seeps in the salt province of the lower Congo basin. Part II: A regional validation

Romain Jatiault, Lies Loncke, Damien Dhont, Dominique Dubucq, Patrice Imbert

Geophysical characterisation of active thermogenic oil seeps in the salt province of the Lower Congo Basin. Part II: A regional validation

Romain Jatiault [a, b]*, Lies Loncke [b], Damien Dhont [a], Dominique Dubucq [a], Patrice Imbert [a]

[a] Total SA, Centre Scientifique et Technique Jean Feger (CSTJF), Avenue Larribau, 64018 Pau, France

[b] University of Perpignan Via Domitia, Centre de Formation et de Recherche sur les Environnements Méditerranéens (CEFREM), UMR 5110, 52 Avenue Paul Alduy, 66100 Perpignan, France

Key words: *Oil slicks, Thermogenic fluid seeps, Pockmarks, Asphalt, Salt diapir, Lower Congo Basin, Gas hydrates, Double BSR*

Abstract

The Lower Congo Basin is known to discharge a substantial volume of oil towards the sea surface, from more than one hundred seafloor seep sites distributed throughout the deep province of the Lower Congo Basin. A large geochemical coring survey confirmed the presence of oil on the seabed. The combination with the seismic data considerably improved the identification of the origin of the oil slicks on the seabed. Multiple specific geophysical characteristics of thermogenic hydrocarbon seep sites were highlighted in a previous detailed analysis of seismic datasets. This study aims to test the characteristics previously identified at regional-scale. The active discharge zone is limited to the distal province of the basin. It is characterized by strong compression / shortening due to the sliding of the post-salt super-sequence, resulting in numerous salt diapirs that control the location of seafloor oil seep sites. The paper describes the bathymetric, reflectivity, amplitude and sub-bottom profiler characteristics of a group of thermogenic seep sites. They correspond essentially to submarine mounds or pockmarks of complex and irregular shape surrounded by hummocky mounds. Active oil pockmarks are systematically associated with positive amplitude anomalies on the seabed and are linked to vertical high-amplitude columns rooted in the seismic reflector and associated with the base of the gas hydrate stability zone. The sub-bottom profiler data shows that the hummocky mounds are connected

by a network of faults to high-amplitude bodies buried under a consistent sediment thickness. Based on the definition of specific geophysical features (seafloor mounds, complex shape and irregular pockmarks, positive anomalies of seafloor amplitude, high-amplitude vertical pipes), we identified a series of potential oil seep sites at basin scale. The mounds are particularly recognizable using the seismic curvature attribute; we have identified 2946 individual hummocks that are grouped in 50 zones with a density of 35 to 240 per km². They are believed to be associated with asphalt storage on the seafloor and related to the biodegradation of heavy oils during hydrocarbon dysmigration through the sedimentary pile. Unusual double BSRs occur over the study area; these are also a specific feature of thermogenic seep sites. Barely half of the potential sites identified on the seismic datasets are associated with recurrent oil slicks at the sea surface. The proportion of remaining anomalies may be associated with inactive seep sites over the period of satellite-based monitoring or gas-dominated seep sites.

1. Introduction

Characterizing the natural transfer of hydrocarbons from petroleum reservoirs to the seafloor has strong implications on the understanding of the evolution of sedimentary basins (***Gay et al., 2006a; Cartwright et al., 2007; Andresen et al., 2011, Anka et al., 2013; Marcano et al., 2013; Serié et al., 2017***), deep marine ecosystems inventories (***Charlou et al., 2004; Ondreas et al., 2005; Jones et al., 2014***) or submarine geohazards (***Bünz et al., 2005; Hill et al., 2011***), see the review by ***Anka et al. (2012).*** Pockmarks are among the most common expression of focused fluid flow at the seafloor (***King and MacLean, 1970; Hovland and Judd, 1988; Judd and Hovland, 2007***). Their size and geometry depend on sediment host properties and hydrocarbon flux (***Hovland et al., 2012***). The ascent of fluids through the sedimentary series causes vertical successions of acoustic anomalies on seismic sections (***Cunningham and Lindholm, 2000; Heggland, 2002; Gay et al., 2006b)***. They are called either pipes, defined as vertical successions of increasing reflection amplitudes (typically narrow, i.e. up to a few 100m diameter) and known to commonly form large clusters, or chimneys, defined as large-scale

(typically > 1 km diameter) and solitary features without any particular internal reflection (***Løseth et al., 2001; Loncke et al., 2004; Cartwright et al., 2007; Løseth et al., 2009; Hustoft et al., 2009; Moss and Cartwright, 2010; Løseth et al., 2011; Ho et al., 2012; Karstens et al., 2015***). In the case of abundant gas migration towards the seabed, hydrates precipitate at the interface between free gas and hydrate domains. This forms a seismic reflector with a polarity opposite to that of the seabed, known as the Bottom Simulating Reflection (BSR) (***Shipley, 1979; Hovland et al., 1997; MacKay et al., 1994; Berndt et al., 2004; Haacke et al., 2007***). The identification of sea surface oil seepage slicks is used throughout the petroleum exploration workflow to validate source rock maturation, from targeting (***Kornacki et al., 1994; Thrasher et al., 1996; Williams and Lawrence, 2002; O'Brien et al., 2005; Stalvies et al., 2017***) to prospect validation (***Jauer and Budkewitsch, 2010***). Positioning the outlines of multi-temporal slicks on the same map commonly shows radiating features from the central source area (***De Beukelaer et al., 2003; Jatiault et al., 2017***). The spatial imagery was able to detect 50% of potential oil-supplying seep sites identified on exploration seismic in the Gulf of Mexico (***Garcia-Pineda et al., 2010***).

Recently, ***Serié et al. (2017***) set out a methodology to study hydrocarbon fluid flow by combining remote sensing, seafloor coring campaign and industrial seismic data. The present study relies on this pre-existing methodology that we complemented with a denser dataset of sea surface natural slicks together with high resolution sub-seafloor data. More recently, ***Jatiault et al. (2019, Part I)*** presented seafloor and sub-seafloor high-resolution characteristics of one active oil seep in the Lower Congo Basin (see details in section 2.2). This complementary study aims at testing the recognition criteria defined for a single oil seep on a larger seep population recognised in the Lower Congo Basin. The combination of sea-surface slicks database, geochemical cores and geophysical anomalies (high-resolution surveys used for geo-hazards evaluation and exploration 3D seismic) made it possible to inventory oil-seep sites over a 35*50 km wide area. The comparison of oil-supplying seeps with the whole set of fluid-flow features at the seafloor and in the shallow subsurface will be used to better discriminate and define seismic features that can potentially be diagnostic of oil seep sites. This study

discusses about the significance of fluid-related seismic features with an updated methodology integrating for the first time sea surface slicks and geophysical data in the Lower Congo Basin. Active oil seep sites will be compared with potential seep sites identified from geophysical attributes in the Lower Congo Basin.

2. The Lower Congo Basin

2.1. Geological setting and petroleum systems

The study area located between 10 to 12 °E and 6 to 8°S corresponds to a large oil-seeping province in deep offshore Angola characterised by water depths ranging from roughly 1000 to 3000 m. The chrono-stratigraphic framework of the LCB is divided into 3 major phases after the South Atlantic opening during the Early Cretaceous (144 - 140 Ma). The pre-salt (Berriasian to Barremian) succession consists of extensive lacustrine deposits including the oil-prone (mix type I/II kerogens) ***Bucomazi Fm*** (Fig. 1c; ***Burwood, 1999; MacHargue, 1990;*** **Schoellkopf** ***and Patterson, 2000; Brownfield and Charpentier, 2006***). The transitional phase (Late Barremian to Aptian) marks the end of the crustal extension followed by a period of thermal subsidence (***Brice et al., 1982; McHargue, 1990; Fort et al., 2004***). The confined environment of the margin together with a drop in the main sea level enabled the deposition of a thick evaporite layer (1000 m thick in average; ***Marton et al., 2000***; Fig. 1b). The post-salt super-sequence is subdivided into three main episodes. The aggrading stage started with the development of a carbonate-ramp (***Pinda Fm;*** 113 - 95 Ma) under stable climatic and restricted marine conditions (***Haq et al., 1987; Séranne, 1999; Séranne and Anka, 2005***). This period continued with a progressive deepening of the basin due to thermal subsidence, leading to the deposition of the oil-prone **Iabe Fm** (99 - 65 Ma, ~10 % TOC; ***Burwood, 1999; Cole, 2000***) and subsequent (~4% TOC) **Landana Fm** (65 - 45 Ma; ***Cole et al., 2000,*** **Schoellkopf** ***and Patterson, 2000;*** Fig. 1c). The pre-salt series are the most prolific source intervals in the basin as Tertiary source rocks are immature over most of it. The Eocene/Oligocene transition corresponds to a period of amplified sea level variations ("Ice house" period; ***Séranne, 1999).*** It is marked by a regional unconformity, corresponding to a 10

Ma hiatus controversially interpreted as originating from the African superswell (***Nyblade and Robinson, 1994***) or climate fluctuations. The 500 m thick eroded series were transported towards the basin (***Teisserenc and Villemin, 1989; Séranne et al., 1992; Anka et al., 2009).*** The prograding stage (35 - 5 Ma) corresponds to the establishment of the paleo-Congo during the early Oligocene. It was coupled with an "ice house" period, resulting in the deposition of siliciclastic sediments (**Malembo Fm**). The Miocene-Pliocene transition is marked by the shift of the Congo River to its present-day location. The development of an important upwelling system during the Early Quaternary (***Uenzelmann-Neben, 1998***) resulted in fining-upward sedimentation, leading to fine-grained deposits in the deep sea fan. The post-salt super-sequence is affected by gravitational deformation, sliding over the Aptian salt décollement layer. Salt tectonics subdivided the basin into an upslope extensional domain, a translated area and a downslope compressive province characterised by salt diapirs, which confined the sedimentation to minibasins (***Oluboyo et al., 2014***).

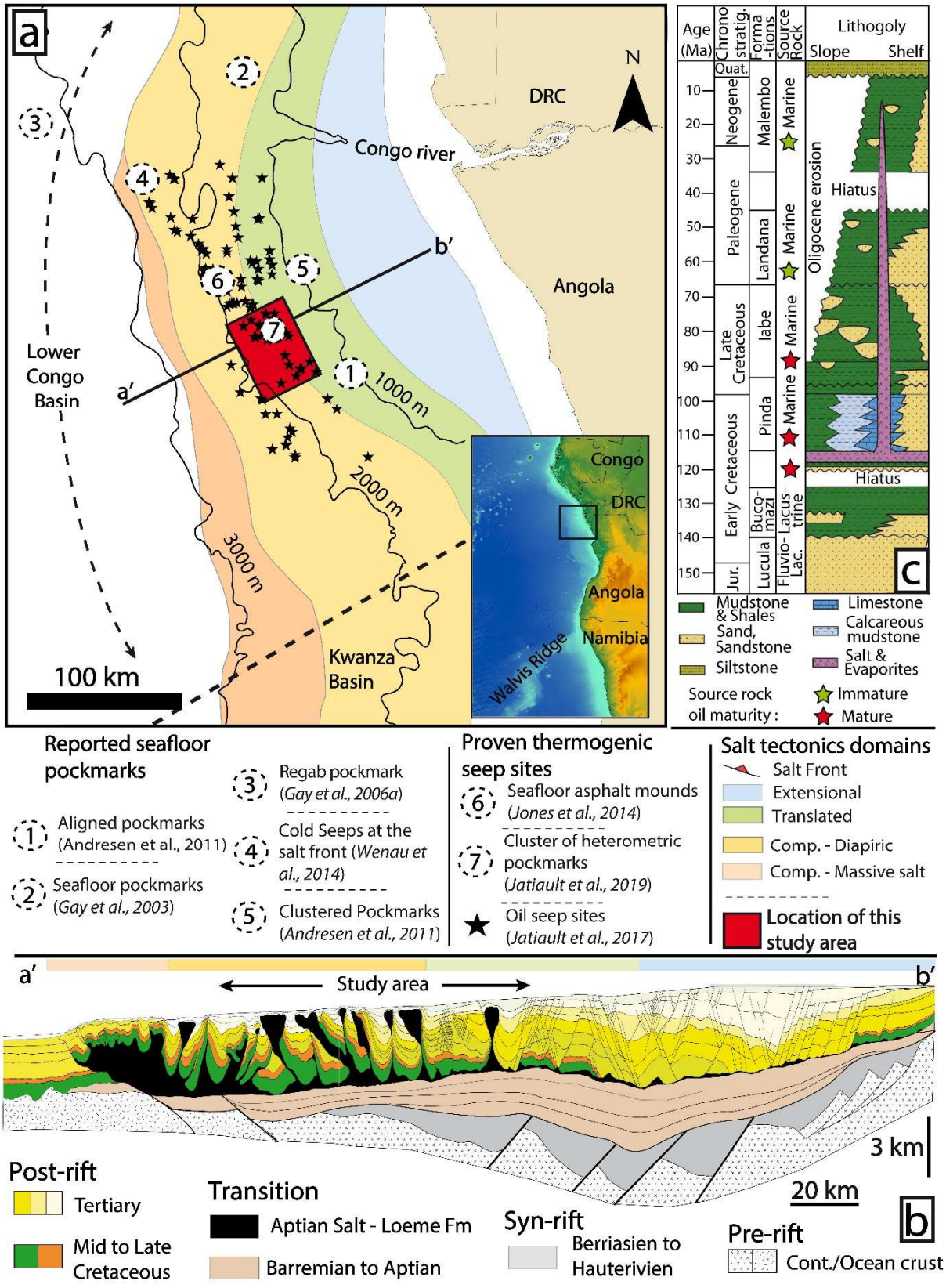

Fig. 1: a. Location map of the study area showing the main geological provinces of the LCB. The map integrates the seafloor seeps reported in the literature (compiled from *Gay et al., 2003; Gay et al.,*

***2006a; Gay et al., 2007; Andresen et al., 2011; Wenau et al., 2014; Jones et al., 2014*) and recurrent oil slicks at the sea surface (black stars, from *Jatiault et al., 2017*). Continuous black lines represent 1000 m isobaths (Gebco). b. Regional cross section across the LCB displaying the pre-rift, syn-rift and post-rift sequences (modified from *Jatiault et al., 2017*). c. Chronostratigraphic log and petroleum system plays (modified from *Anka et al., 2013*).**

2.2. Literature review of natural hydrocarbon seeps

The LCB is affected by a large active fluid seepage system, as revealed during intensive petroleum exploration over the last decade. Seabed outcrops of Miocene series, characterised by extensive high amplitudes above the crest of the salt diapirs, correspond to preferential stratigraphic pathways for migrating fluid in the salt provinces (***Serié et al., 2017***). In the salt minibasins, widespread classical type I pockmarks (Conical; see definition of Type I in ***Riboulot et al., 2016***) related to sediment pore dewatering and biogenic methane venting are associated with the polygonal fault networks (***Cartwright 2007; Andresen et al., 2011***). Aligned type I pockmarks commonly follow the maximal flexural syncline axis of the minibasins (No. 1 in Fig. 1a; ***Andresen et al., 2011***) or occur as sinuous trends marking the ancient pathways of the Congo canyon (No. 2; ***Gay et al., 2003***). A biogenic origin is also suspected for the giant (~2000m diameter) Regab pockmark, located in the deep abyssal plain at a water depth of 3150m (No. 3; ***Gay et al., 2006a***). The origin of the gas expelled at the salt front remains undetermined (No. 4; ***Wenau et al., 2014***). A thermogenic contribution is highly suspected for isolated pockmarks linked with Miocene turbidite channels (No. 2; ***Gay et al., 2006 b***) and for clustered pockmarks linked with salt diapirs (No. 5; ***Andresen, 2012***). The migration of thermogenic hydrocarbon is proven from the identification of a large number of seafloor asphalt mounds that spread on top of salt diapirs (n°6; ***Jones et al., 2014***). Seafloor asphalt mounds may reach approximately 1m in height and host an abundance of biofauna. From the analysis of spaceborne SAR imagery, ***Jatiault et al. (2017***) calculated that the 100 oil seep sites of the compressive salt domain (black stars in Fig. 1a) emit a volume of $4.38*10^6$ litres of oil per year

141 The vertical association of sea-surface slicks and seafloor data show that seafloor seeps correspond to
142 clusters of pockmarks and seafloor mounds (n°7; ***Jatiault et al., 2019, Part I***). One pockmark cluster
143 investigated in detail in ***Jatiault et al., 2019, part I*** consists of a complex of heterometric depressions
144 associated with asphalt mounds with diameters of 10 to 15 m in on the seafloor (***Unterseh et al., 2013;***
145 ***Jones et al., 2014***). The subsurface is affected by several geophysical features including a shallow High
146 Impedance Layer (HIL) that reaches the seafloor at the location of depressions on the sub-bottom
147 profiler data. The HIL is interpreted as related to carbonate concretions with a possible contribution of
148 asphalt layers (***Hill et al., 2011***), (2) a set of two parallel reflections, about 50 ms apart, whose polarity
149 is opposite that of the seafloor. They are interpreted as a methane-related BSR overlying a second BSR
150 that could be related to a mix of heavier gas (***Jatiault et al., 2019***), (3) two different positive amplitude
151 anomalies horizontally delimited by the BSR; massive high-amplitude bodies below and vertical pipes
152 that connect the BSR with the seafloor above.

153 # 3. Data and Methods

154 This study adopts the methodology of ***Serié et al. (2017)*** to characterize the fluid flow phenomena in
155 the Kwanza basin. We refined it by integrating a detailed slicks inventory together with AUV-based
156 sub-bottom profiler data. Precise location of oil slicks origins at the sea surface better locates the
157 location of the active seeping vents at the seafloor (***Jatiault et al., 2017***) and to evaluate the seepage
158 activity. In addition, the SBP provides greater discrimination between seafloor fluid-related
159 morphotypes and shallow acoustic anomalies. All the maps shown in this publication (Fig. 3a, b; Fig.
160 6a, b; Fig. 7f; Fig. 9a, b and Fig. 11 a, b) cover the exact same area (red square location in Fig. 2) which
161 has been upscaled to enhance the quality of maps although the study was conducted over a larger
162 area that corresponds to the province imaged with 3D seismic.

163 ## 3.1. SAR data and seepage slicks inventory

164 The entire SAR collection consists of long-range monitoring integrating 156 scenes acquired over 21
165 years. The variability of the SAR acquisition data distribution is high, both temporally and spatially, as

166 seen in Table 1 and Fig. 2, respectively. The oil-seeping province is imaged with a stack of SAR scene
167 collection varying from 50 to 150 overlapping scenes (Fig. 2). The SAR dataset consists of a combination
168 of X-band (wavelength of 2.5 to 3.75 cm) and C-band (3.75 to 7.5 cm) data that are known to be the
169 most suitable wavelengths to detect oil slicks at the sea surface, enabling the recognition of the
170 thinnest oil films (***Gade and Alpers, 1998***). The oil at the sea surface reduces the wind-induced capillary
171 waves, thereby locally decreasing the radiometric values on SAR data. The discrimination of look-alikes
172 (i.e. platform or boat spill, low wind effects, algal blooms) is primarily based on object features
173 (radiometric values, edge sharpness and sinuosity), the remaining potential seepage slicks database is
174 stacked on a compilation map. The variable orientation of surface slicks controlled by the sea surface
175 water displacement (wind and currents) creates diverging patterns whose centres identify the oil
176 surfacing area (black stars in Fig. 2; ***Jatiault et al., 2017***). The proximal terminations of individual slicks
177 in the oil surfacing area are called Oil Slick Origins ***(OSO; Garcia-Pineda et al., 2010***). When there is no
178 predominant current, the vertical projection of the average location of the OSO on the seafloor
179 provides the most accurate location of the source on the seafloor.

180 **Table 1 : Inventory of SAR scenes collection characteristics.**

Satellite/ Sensor	Period of imagery	Wavelength	Pixel Spacing (m)	Amount of SAR data
Envisat /WSM	2002 - 2012	C (5.8 cm)	75	46
ERS/IMP	1994 - 2001	C (5.8 cm)	12.5	17
Cosmo-SkyMed	2009 - 2014	X (3.1 cm)	3-15	80
TerraSAR – X	2011	X (3.1 cm)	20	6
RADARSAT-2	2005 - 2012	C (5.3 cm)	25-50	7

181 ## 3.2. Geochemical coring

182 The seafloor coring campaign was based on regional 2D seismic sections, across the deep
183 transitional/compressive province of the LCB (blue triangles in Fig. 2). Piston cores were collected prior
184 to the acquisition of high resolution 3D seismic presented in this paper. The entire dataset consists of

488 piston cores recovered during several coring campaigns between 1998 and 2010 by TDI Brooks. The piston cores consist of a vertical succession of 20 cm-long sub-sections with a maximum depth of 5.6 m. The geochemical analyses include:

- Gas Chromatography - Mass Spectrometer (*GC - MS*) which provides the distribution of alkane composition (Sn alkane) assessed from the retention time (performed for 423 cores out of the whole set). The sum of individual extractible alkane portions provides an estimation of the concentration of high molecular-weight hydrocarbon (C_{15+} hydrocarbon concentration).
- Unresolved Complex mixture (UCM) defined as the unextractable organic carbon with chromatogram (C_{15+}).
- Total Scanning Fluorescence (TSF) intensity measured with spectrometry technique, which helps quantify the fluorescence of aromatic components (***Abrams, 2005***). The maximum intensity (*I max*) corresponds to the maximal values of fluorescence between emission (*EM*) spectrum and excitation (*EX*) spectrum (e.g. ***Barwise and Hay, 1996***). The ratio (R_1) between maximal value of EM and EX provides an indirect estimation of °API (American Petroleum Institute; API gravity = $- 0.1*R_1 + 59.8$).

200 - D

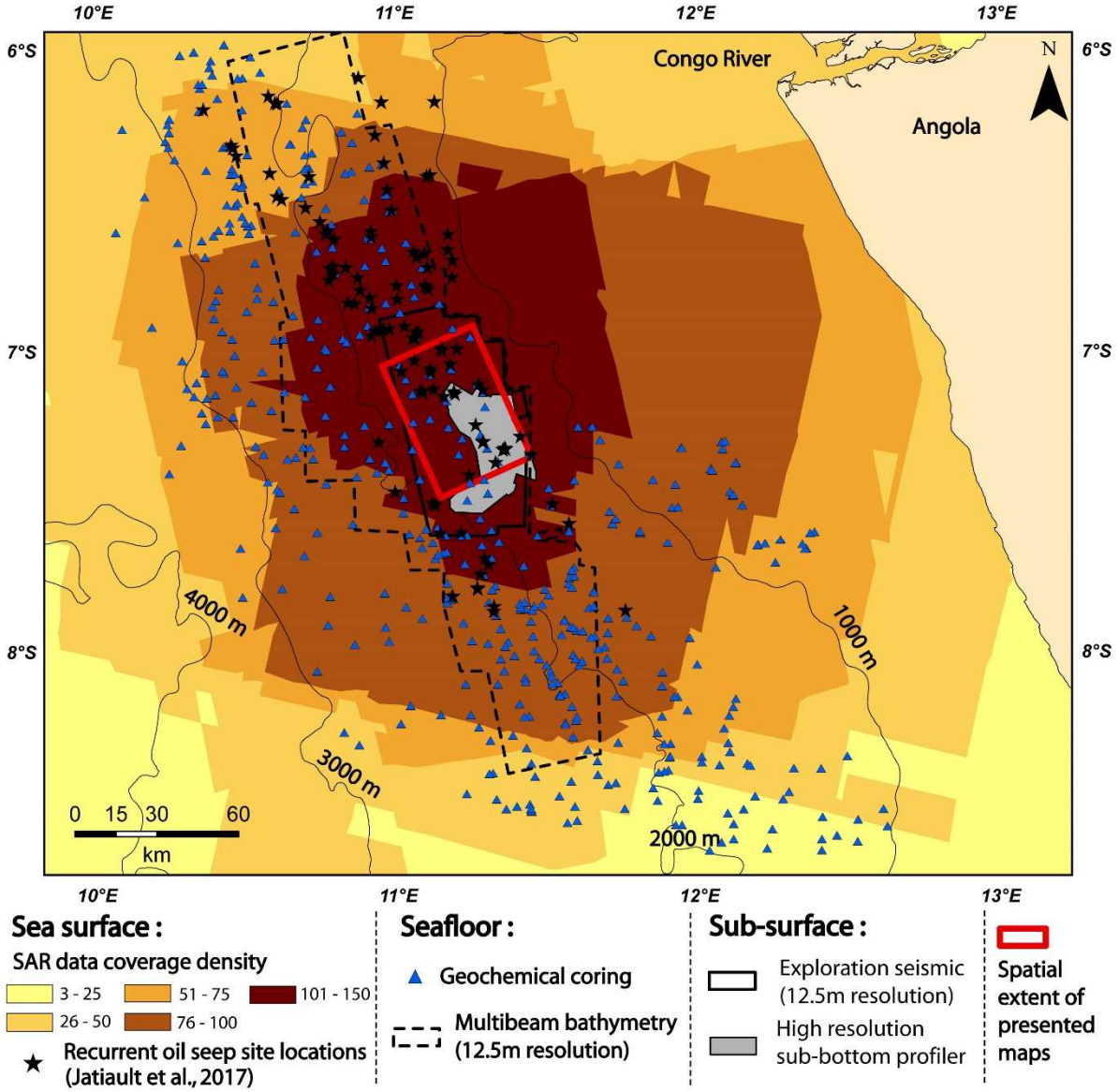

201

202 **Fig. 2: Geographical localisation of the study area and compilation of available dataset. The red**

203 **square refers to the spatial extent of maps displayed in Fig. 3a, b; Fig. 6a, b; Fig. 7f; Fig. 9a, b and Fig.**

204 **11 a, b.**

205 ### 3.3. Seismic dataset

206 The available seismic dataset consists of a 3D seismic cube used for petroleum exploration,

207 complemented by a high-resolution survey used for geo-hazards evaluation acquired with an

208 Autonomous Underwater Vehicle (AUV).

Table 2 : Characteristics of the available datasets including seafloor and sub-seafloor imagery.

Data type		Line spacing (m)	Maximum Penetration (ms TWT)	Dominant frequency	Horizontal Resolution	Vertical Resolution	Covered area
Sub-seafloor	3D exploration seismic	12.5*12.5	4500	20 - 100 Hz	12.5 m	~4 m	3300 km²
	AUV Sub-bottom profiler	175*1000	100	1.5 - 4.5 kHz	1.5 m	~10 cm	5500 km²
Seafloor	Multibeam	-	-	12.5 kHz	12.5 m	-	16 000 km²
	AUV HR bathymetry	-	-	200 kHz	1.5 - 3 m	-	830 km²
	AUV Seafloor Reflectivity	175*1000	Few centimetres	120 - 410 kHz	3 m	-	830 km²

The seismic cube covers a 3300 km² area with a maximum record length of 4500 ms TWT (Fig. 2). The source system is composed of two airgun clusters, 50 m separated with shot interval of 25 m. The sensor system consists of 10 parallel, 100 m separated streamers, and composed of 396 individual receiver groups separated by 25 m. We used the near-offset seismic trace.

The Sub-Bottom Profiler (SBP) dataset followed a grid with a line spacing of 1000m in the slope direction and 175m in the strike direction, and was acquired in two surveys operated in 2009 by C&C and in 2011 by Fugro (Table 2). The combination of the two datasets consists of an 830 km² gridded area and 5500 km of SBP sections. The high-frequency SBP is characterised by a 10 cm vertical resolution whereas the penetration is limited to the first 100 ms TWT below seafloor. We used the amplitude attribute to display the 3D seismic impedance contrast at lithological interfaces. The RMS (Root Mean Square) amplitude was used to display SBP sections and to identify geophysical anomalies on 3D seismic. Seafloor curvature maps are computed from the first arrivals of the 3D seismic cube, using a window size of 3 profiles and an interpolation length of 5 samples.

The high-resolution survey includes bathymetry (EM2000 multibeam echo-sounder) and seafloor reflectivity acquired along the acquisition tracklines of the vehicle. In areas not surveyed by the AUV, lower-resolution seafloor data (bathymetry, seismic amplitude) were taken from the seafloor reflections picked on the 3D seismic using Sismage software (***Guillon and Keskes, 2004***). In addition,

the seafloor origin of a large majority of (>80 %) of recurrent oil seep sites were imaged at large scale (16 000 km²), 12.5m resolution multibeam bathymetry. The computation of the slope map with superimposed seafloor isochrones enhances the imagery of seafloor features. Seafloor curvature maps are computed from the first arrivals on the seafloor, extracted from the 3D seismic cube using Sismage software and taking estimation window size of three samples and an interpolation length of five samples.

4. Analyses and results

4.1. Evidence of active oil seeps

4.1.1. Sea surface manifestations of oil presence

The visual analysis of the 156 SAR scenes revealed more than 3000 seepage slicks characterised by elongated/curvilinear trends with variable length (Fig. 3a). Diverging black streaks and OSO concentration area within point clusters were used to identify active oil seep sites. The oil seepage system consists of more than 100 seep sites distributed on the deep part of the Miocene Congo deep-sea fan for water depths between 1200 to 2700 m. Observations of multi-temporal oil slicks at the sea surface vary from 5 to 80 % from one seep site to another. The radius of the spatial scatter of OSO for individual sea bottom seepage points has a mode radius of 750 m (***Jatiault et al., 2018***), suggesting that the lateral deflection due to underwater currents remains low compared to the water depth (Fig. 3b; ***Jatiault et al., 2019, Part I***). The vertical projection of OSO locations, the density and the geometric mean centre coincide vertically at 98 % with seabed morphological anomalies, confirming the absence of permanent deflection in the water column, which helps to identify active oil seep sites nearly at the apex of OSO locations (Fig. 3c, d, and e).

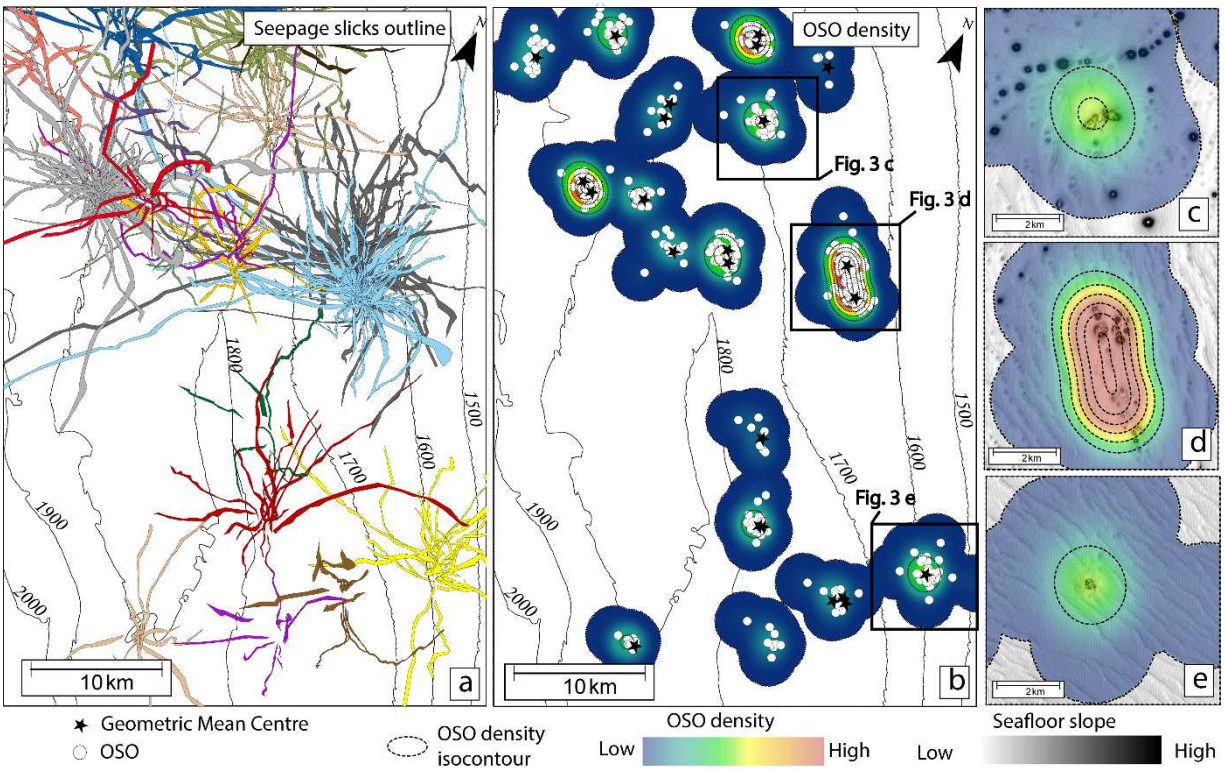

Fig. 3: a. Compilation map of seepage slick outlines identified from the interpretation of 156 overlapping SAR scenes. The colour corresponds to distinct active oil seep sites. b. Compilation of OSO pinpointed from diverging recurrent slicks in white dots, superimposed with the OSO density map and iso-contour. High values in warm colours correspond to frequent oil surfacing areas. c, d, e. Details of the OSO density map at frequent oil surfacing locations, superimposed in transparency with slopes map of the seafloor.

4.1.2. Seafloor geochemical coring

The hydrocarbon content of seafloor piston cores is strongly variable (Fig. 4a). Geochemical analysis of heavy (C_{15+}) hydrocarbons shows that the sum of alkane (*Sn*) concentration (C_{16} - C_{32}) ranges from 0.1 to 36 ppm while the concentration of UCM varies from 2 to 85 000 ppm. While the fluorescence (TSF) intensity changes from 1 116 to 87 240 000, 35 % of the cores have greater values than the regional background defined at 10 000 units (***Serié et al., 2017***). The plot of fluorescence vs. C_{15+} concentration is an indirect method for quantifying the presence of heavy hydrocarbons in sub-surface sediments (Fig. 4a).

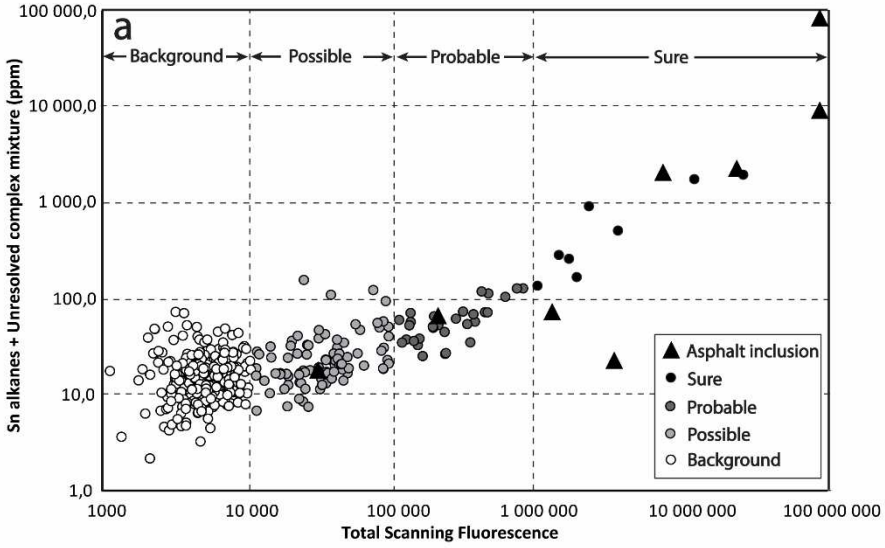

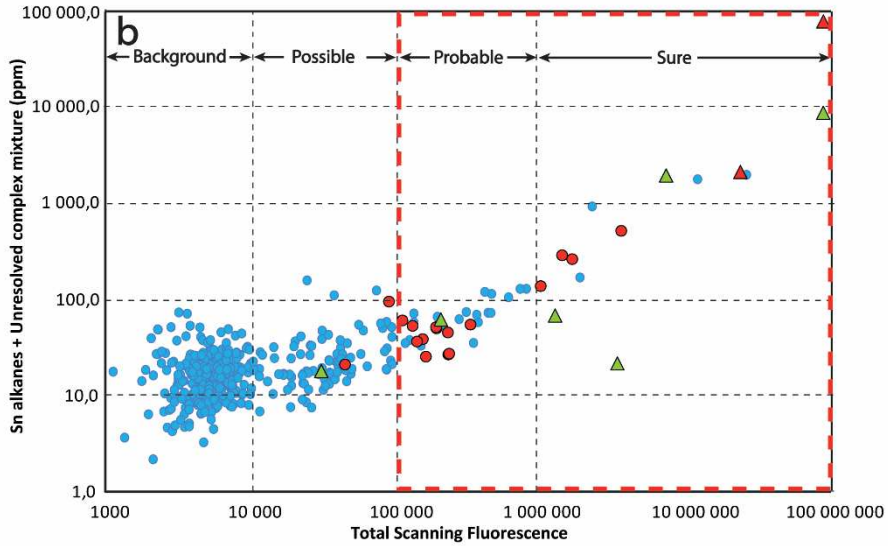

Space-borne / Geochem.	No asphalt inclusion in cores	Asphalt inclusion in cores
No oil slicks at the sea surface	No oil slicks and no asphalt inclusion	No oil slicks with asphalt core inclusion
Sea surface oil slicks	Oil slicks without asphalt core inclusion	Combination of oil slicks and asphalt inclusion

263

264 **Fig. 4: a. Graph (logarithmic scale) of the concentration of the high molecular-weight hydrocarbons**
265 **(C_{15+}) compared to the maximal intensity of the Total Scanning Fluorescence (TSF Imax); the circles**
266 **colours reflects the uncertainty on the presence of hydrocarbons in cores. b. Same graph with color-**
267 **coded symbols to show the correlation with sea-surface slicks; symbols are classified into 4**
268 **categories depending on the geographical correspondence of oil at the sea surface (red circles) and**
269 **visual inclusion in cores (triangles). The red dashed rectangle delimits the two categories "Sure" and**
270 **“Probable” that we consider reliably contain oil traces.**

We considered that hydrocarbon traces are reliably present in cores for TSF values at least 100 times greater than the regional background (Levaché, pers. com). Occurrence of hydrocarbons is possible for 114 cores (TSF values less than 100 000, Fig. 4a). For 38 cores, hydrocarbon traces are probable when the TSF intensity is at least 10 times greater than the regional background (100 000 < TSF < 1 000 000). The presence of hydrocarbon is qualified as being sure for 20 cores having TSF values greater than 10^6.

The observation of asphalt inclusions for 10 piston cores also confirms the migration of oil towards the seafloor (black triangles in Fig. 4a). Even if they represent only 2% (10/488) of the total core array, they correspond to the highest TSF and UCM values.

4.2. Fluid flow features on the seafloor

Seafloor features that may be related to fluid venting are categorised into 7 main families: conical pockmarks (isolated and lined-up), seafloor gullies, complex-shaped pockmarks (clusters of heterometric pockmarks and irregular isolated pockmarks), submarine mounds and scattered positive topographic hummocky features (Fig. 5).

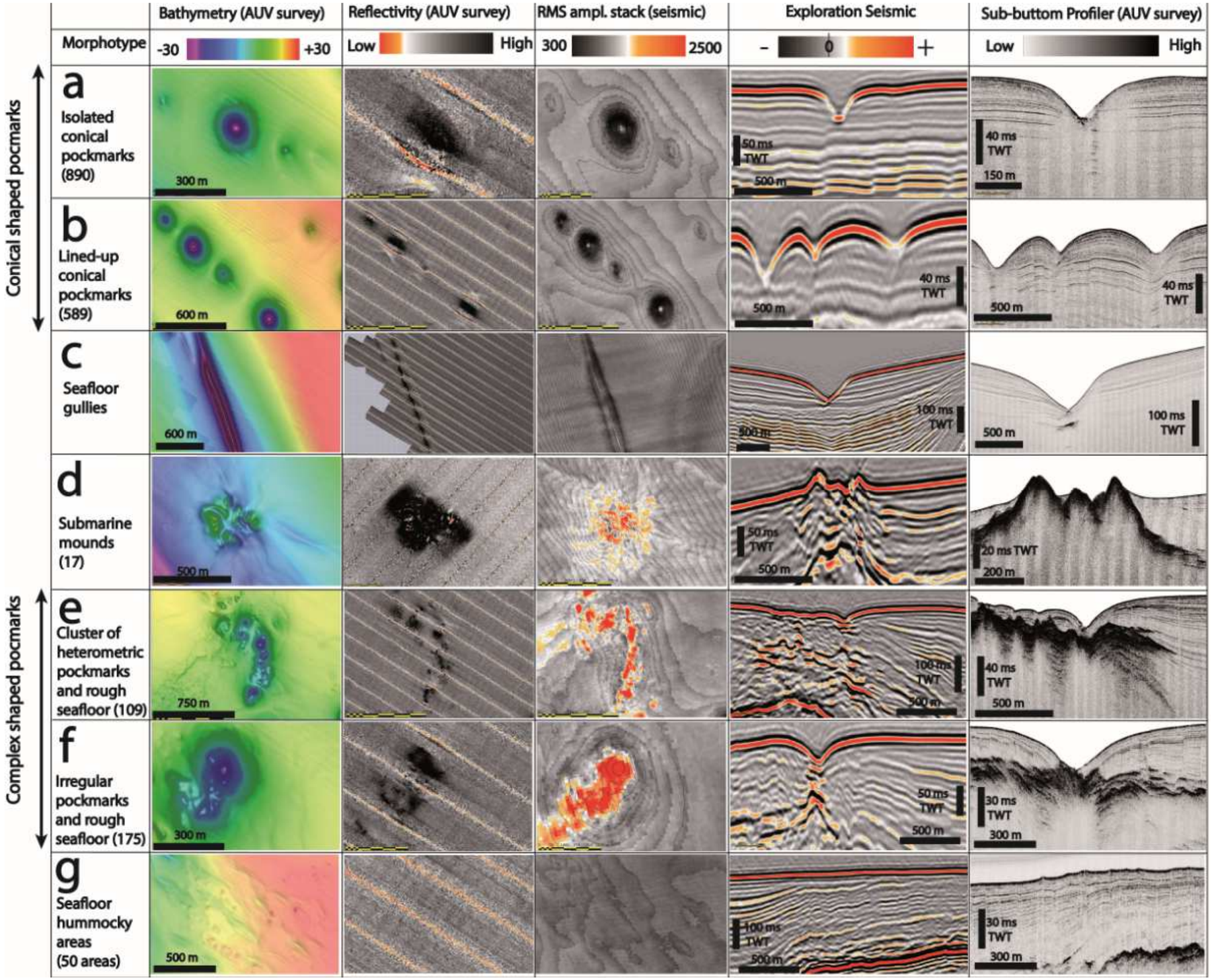
Bathymetry (AUV survey)
Reflectivity (AUV survey)
RMS ampl. stack (seismic)
Exploration Seismic
Sub-buttom Profiler (AUV survey)
Morphotype
-30
+30
Low
High
300
2500
–
0
+
Low
High
Conical shaped pocmarks
a
Isolated conical pockmarks (890)
300 m
50 ms TWT
500 m
40 ms TWT
150 m
b
Lined-up conical pockmarks (589)
600 m
500 m
40 ms TWT
500 m
40 ms TWT
c
Seafloor gullies
600 m
500 m
100 ms TWT
500 m
100 ms TWT
d
Submarine mounds (17)
500 m
50 ms TWT
500 m
20 ms TWT
200 m
Complex shaped pocmarks
e
Cluster of heterometric pockmarks and rough seafloor (109)
750 m
100 ms TWT
500 m
40 ms TWT
500 m
f
Irregular pockmarks and rough seafloor (175)
300 m
50 ms TWT
500 m
30 ms TWT
300 m
g
Seafloor hummocky areas (50 areas)
500 m
100 ms TWT
500 m
30 ms TWT
300 m

285

Fig. 5: Compilation of major fluid vents morphotypes observed on the seafloor in the Lower Congo Basin. The bathymetric colour scale was normalised with a 60 m dynamic range to better distinguish the different morphologies. High amplitudes are displayed in black on the reflectivity map and in red on the seafloor amplitude extracted from 3D seismic.

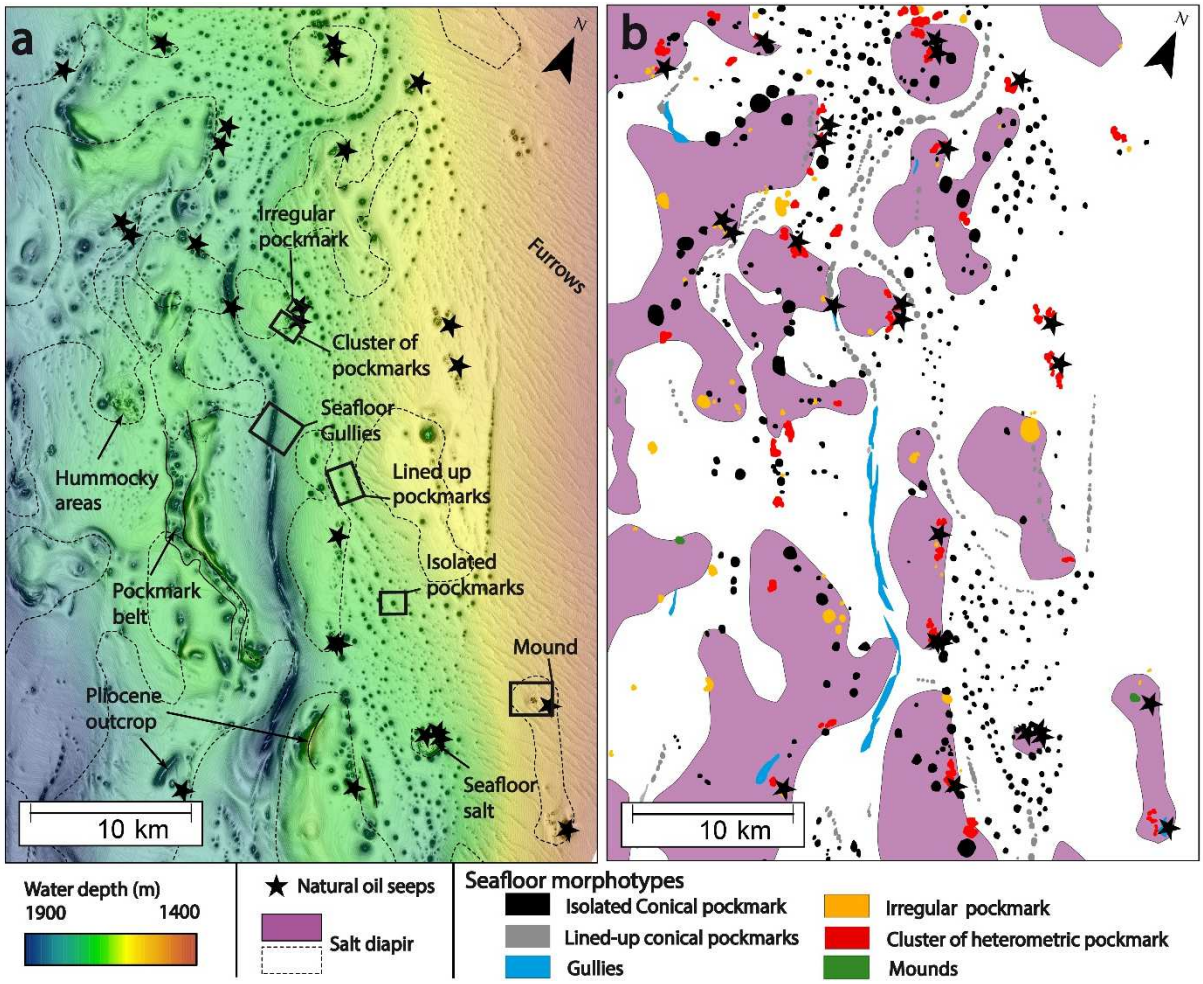

Fig. 6: a. Map of the seafloor (dip + isochron) showing the distribution of fluid flow features. b. Interpretative map of focused fluid flows sorted according to their morphotypes. Black stars show the positions of the mean impact points of oil slicks at the sea surface.

4.2.1. The conical pockmark-gully continuum

Conical pockmarks can reach km-scale diameters with maximum depth of 150 m and are characterized by gentle slopes of ~15° (Fig. 5a). With a total number of 890, they are widespread throughout the study area and mostly occur in salt minibasins (Fig. 6).

298 Lined-up conical pockmarks (Fig. 5b), defined as a succession pool of at least 3 conical pockmarks along
299 a main direction, occur in 3 main settings. First, they are sparsely distributed along the maximal flexural
300 axis of salt minibasins (Fig. 6). Increase of their number and density can ultimately lead to form
301 curvilinear gullies (Fig. 5c) corresponding to deep (>50 m) and elongated (> 1 km) incised depressions
302 on the seafloor. Second, conical pockmarks can occur at the tip of normal faults on the seafloor in
303 association with the sagging of minibasins. Third, they are located at the seafloor interface
304 unconformity between uplifted slabs of Miocene-Pliocene series at diapirs and Quaternary siltstones
305 in minibasins. The total amount of conical pockmarks, including isolated ones and aligned sets, is
306 significant in the study area (1 750 individual features) (Table 3), which represents 85% of the total
307 fluid escape features identified on the bathymetric data.

308 ***4.2.2. Submarine mounds***

309 Submarine mounds are bathymetric highs on the seafloor with a typical relief of 5 to 20m above the
310 surrounding seabed and diameter up to 500m (Fig. 5d). We identified only 17 such mounds; the only
311 one of these that is imaged on HR data appears as a cluster of smaller individual mounds, whose slopes
312 range from 10 to 30°. The high-resolution bathymetry map reveals fault sets diverging radially away
313 from the seafloor mounds; similar radial patterns have been observed around salt diapirs by
314 ***Carruthers et al. (2013)***. Submarine mounds are clearly discernible on the seafloor as patches with
315 higher reflectivity compared to the surrounding seabed, indicating that they are formed of higher
316 impedance material than the background silts and clays. Seafloor mounds are located above
317 allochthonous salt diapirs like the irregular pockmark clusters (Fig. 5). Most of the submarine mounds
318 are associated with spiky diapirs (needle-shaped salt protrusion), and have not been observed above
319 bulbous ones. No clear distinction in terms of seepage proficiency (occurrence rate) could be
320 established between submarine mounds and other active features.

321 ***4.2.3. Complex shaped pockmarks***

322 Complex-shaped pockmarks are uneven fluid escape features on the seafloor with a main depression
323 whose depth does not exceed a few tens of meters. Complex-shaped pockmarks occur as two

distinctive patterns; (1) Clusters of heterometric pockmarks (Fig. 5e), defined as an aggregation of a large number of unit pockmarks (***Hovland et al., 2010***), with clusters reaching 2-3 km and exceeding 1500m in length (***Jatiault et al., 2019, Part I***). They usually develop along the salt-related fault networks at the rim of a salt canopy, thereby creating a complex-shaped depression at broader scale, that contains different heterometric pockmarks; (2) Irregular pockmarks (Fig. 5f), corresponding to sub-circular depressions with a rough aspect at the base. Local depressions are associated with a strong high-amplitude anomaly on the seafloor reflectivity map (Fig. 5). In contrast with previously described mounds, they are mostly found along landward flanks of bulbous diapirs, and never appear in association with spiky ones. We identified 109 clusters of heterometric pockmarks and 175 irregular isolated pockmarks.

4.2.4. Seafloor hummocky areas

The seafloor is affected by rough patches clustering over limited-size areas (10-15m in diameter and few meters high), on top of salt diapir. They were identified on high-resolution bathymetry maps and therefore remain below the 3D seismic resolution (Fig. 7a). However, seafloor hummocky induces a slight disturbance in the seafloor creating a rough aspect that may be discernible from the exploration seismic resolution using specific seismic attributes such as seabed curvature (Fig. 7a). On the HR bathymetry, hummocky areas consist of a numerous small hummocks (Fig. 7b). The discrimination of hummocky features is particularly enhanced using the curvature attribute that measures the bathymetric slope inflexions (Fig. 7c). On curvature maps, hummocky features are characterised by a central (round or elongated; Fig. 7d) high positive value over topographic features, surrounded by sub-circular medium values (~0) and by negative values at the rim (Fig. 7e).

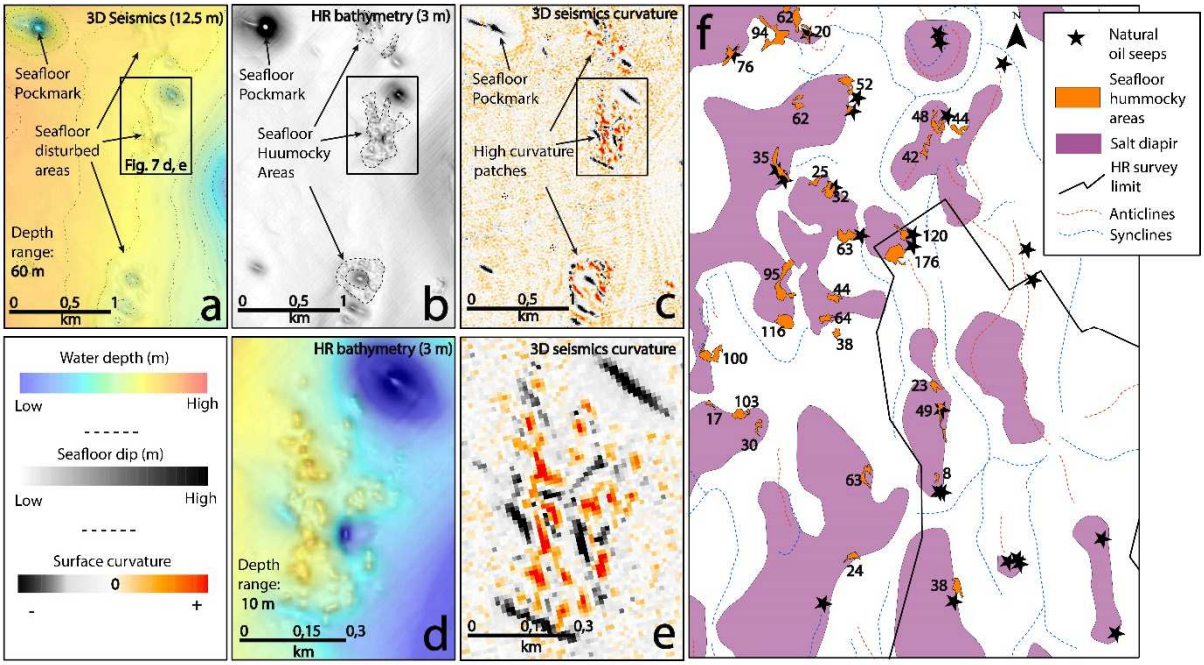

345

346 **Fig. 7: a. Seafloor map from 3D seismic, the dynamic range of the seafloor colour scale is 60 m. b.**
347 **Seafloor slope map of the 3m resolution multi-beam echo sounder affected by the meter-scale**
348 **seafloor hummocky areas. c. Curvature map of the seabed from the 3D seismic data. d. Zoom of the**
349 **3m resolution echo-sounder seafloor map (bathymetric range is 10 m) superimposed with the slope**
350 **map. e. Zoom of the seabed curvature map from the 3D seismic data. f. Geographical inventory of**
351 **the hummocky areas superimposed with salt diapir locations and natural oil seep sites. The numbers**
352 **refer to the amount of detected individual hummocks.**

353 We assumed that rough patches correspond to zones with a high density of seafloor hummocks and
354 individual positive sub-circular features correspond to individual hummocks. The presence of
355 hummock clusters is associated with complex-shaped pockmarks (clusters of heterometric and
356 irregular pockmarks) in most cases. Underlying HIL remains buried under few tens of ms below the
357 seafloor and connected to hummocks by shallow faults (Fig. 5g). We identified 2946 possible individual
358 hummocks over the area imaged with 3D seismic. Ten areas with a high hummock concentration were
359 identified on the HR survey and an additional 50 on the wider 3D survey (12.5m resolution) (Fig. 7). 3D
360 seismic data detects about 55% of individual hummock features visible on the HR survey. The number
361 of discernible hummock features in clusters ranges between 10 to 210 on the 3D seismic, covering

surface areas from 0.12 to 3.45 km² and corresponding to a density of 35 to 240 hummocks per km². One piston core was drilled inside a hummocky cluster visible on the 3D seismic and showed asphalt inclusions in the sediment. Hummocks have the same morphology and geophysical characteristics as asphalt mounds and their distribution is similar to that of those previously identified in the area (***Unterseh et al., 2013; Jones et al., 2014***). Seafloor hummocks are interpreted as seafloor asphalt storage that reached the seafloor through scattered emission points above the crest of salt diapirs, following a stage of oil migration across sedimentary series.

4.3. Seismic geomorphology in the sub-surface

4.3.1. Positive geophysical anomalies on the 3D seismic

We computed the RMS amplitude stack of the first 100 ms TWT below the seafloor reflection to identify geophysical anomalies (Fig. 8 A). Geophysical anomalies occur as three main distinct features, or categories.

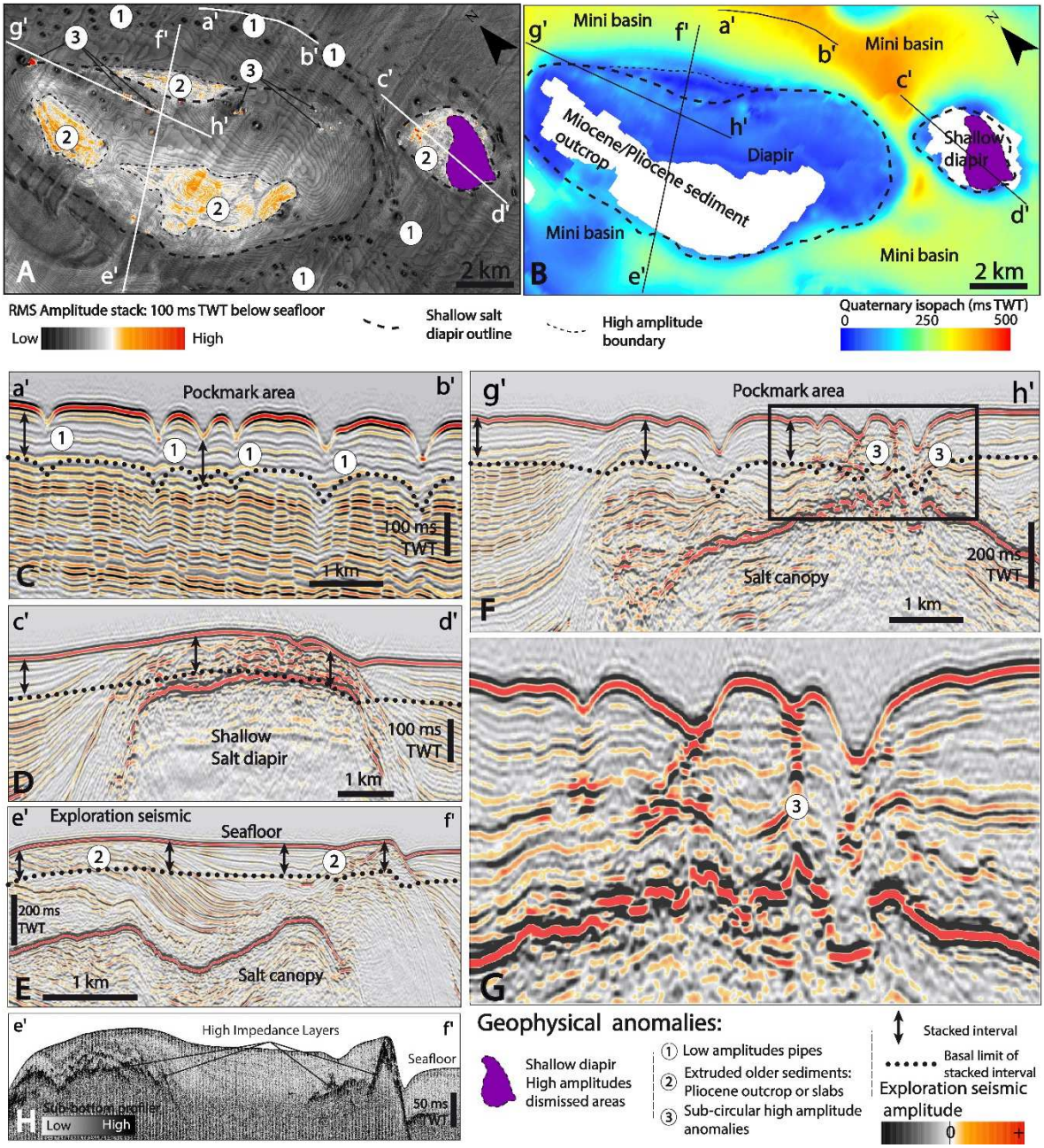

374

375 **Fig. 8: A. Map of amplitude root mean square (RMS) over the first 100 ms TWT below seabed,**
376 **showing four types of seismic anomalies. The dotted ellipse is the outline of a shallow diapir that**
377 **coincides with consistent high amplitudes close to the seafloor, the outcrop of Neogene series that**
378 **creates a moderate amplitude anomaly, the sub-circular low amplitude anomaly in minibasins and**
379 **smaller sub-circular high-amplitude anomalies associated above salt diapirs. Please note that the**
380 **North arrow has been rotated to ensure optimal visibility. B. The quaternary sediment isopach**
381 **reveals the differential sedimentation between minibasin area and diapir area. C, D, E, F. Seismic**

sections through the different geophysical anomalies identified on fig. 8A (see details in text and locations on the Fig. 8 A, B). G. Zoom of from section F on high-amplitude pipes. H. SBP section across the High Impedance layer.

Above shallow salt diapirs, the RMS interval cross-cuts the top of salt, making high-amplitude anomalies that are unrelated to fluid effects. We dismissed these areas from the interpretation (purple patches in Fig. 8).

The first type of acoustic anomaly (1 on Fig. 8 A) is defined as a vertical succession of low-amplitude reflections. Low-amplitude pipes suggest acoustic dimming in the sedimentary pile where the impedance contrasts are attenuated across successive lithologic interfaces. Low-amplitude pipes are essentially spread across salt minibasins or aligned along the maximal flexural axis of salt minibasins (Fig. 8 A; Fig. 9). We identified a large number of low-amplitude pipes (582) across the area imaged using the exploration seismic (Fig. 9). The low-amplitude anomalies identified on the 3D seismic correspond to the locations of conical shaped pockmarks (isolated and aligned) and gullies (Fig. 8 C). The lithologic interfaces are disrupted by an acoustically transparent zone in the sub-bottom profiler below the location of conical pockmarks (Fig. 5). Lithologic interfaces are either truncated by the seafloor depression or associated with a slope inflection, stacked on successive lithologic interfaces. In the former case, the active fluid seep probably corresponds to a recent initiation of the seepage activity. In the latter case the deepest interval affected can be followed down to 600 ms TWT on the exploration seismic. On the sub-bottom profiler, stratigraphic boundaries surrounding the low-amplitude anomalies remain well organised down to the acoustic penetration. Most correspond to the bulls-eye pockmarks defined by ***Andresen et al. (2011)***.

The second type (2; Fig. 8 A) of acoustic anomaly corresponds to moderate positive amplitude anomalies related to outcropping older sediments (mostly Neogene) above salt diapirs; these anomalies gradually dim out laterally (Fig. 8 E). Affected areas range from 1 to 10 km². Moderate amplitude anomalies are composed of consistent, extensive patches indistinctively downslope or

upslope (Fig. 8 E) in relation to the depocentre shift/tectonic inversion (***Quirk and Pilcher, 2012***). Uplifting of older sediments can also be detected on the sub-bottom profiler sections where they occur as strong threadlike reflections (Fig. 8 F).

The third type (3; Fig. 8 A) of acoustic anomaly corresponds to local, sub-circular and Positive High Amplitude Anomalies (PHAA; ***Ho et al., 2012***) that are vertically stacked on successive lithologic interfaces, marking a vertical succession of strong impedance contrasts (bright anomalies; Fig. 8 G). The PHAA diameters vary from 60 to 350m and occur either as multiple vertical pipe clusters (see ***Jatiault et al., 2019, Part I***) or isolated chimneys (Fig. 8 G). We identified 75 individual PHAA on the RMS amplitude stack of the first 100 ms TWT, mostly associated with diapirs (Fig. 9). They tend to congregate along the upslope salt flank or minibasin edges. High-amplitude vertical pipes are mostly associated with strong RMS amplitude in the central area surrounded by a moderate amplitude peripheral anomaly. The seafloor expression of PHAA corresponds essentially to the complex shaped pockmarks (clustered or isolated) and submarine mounds.

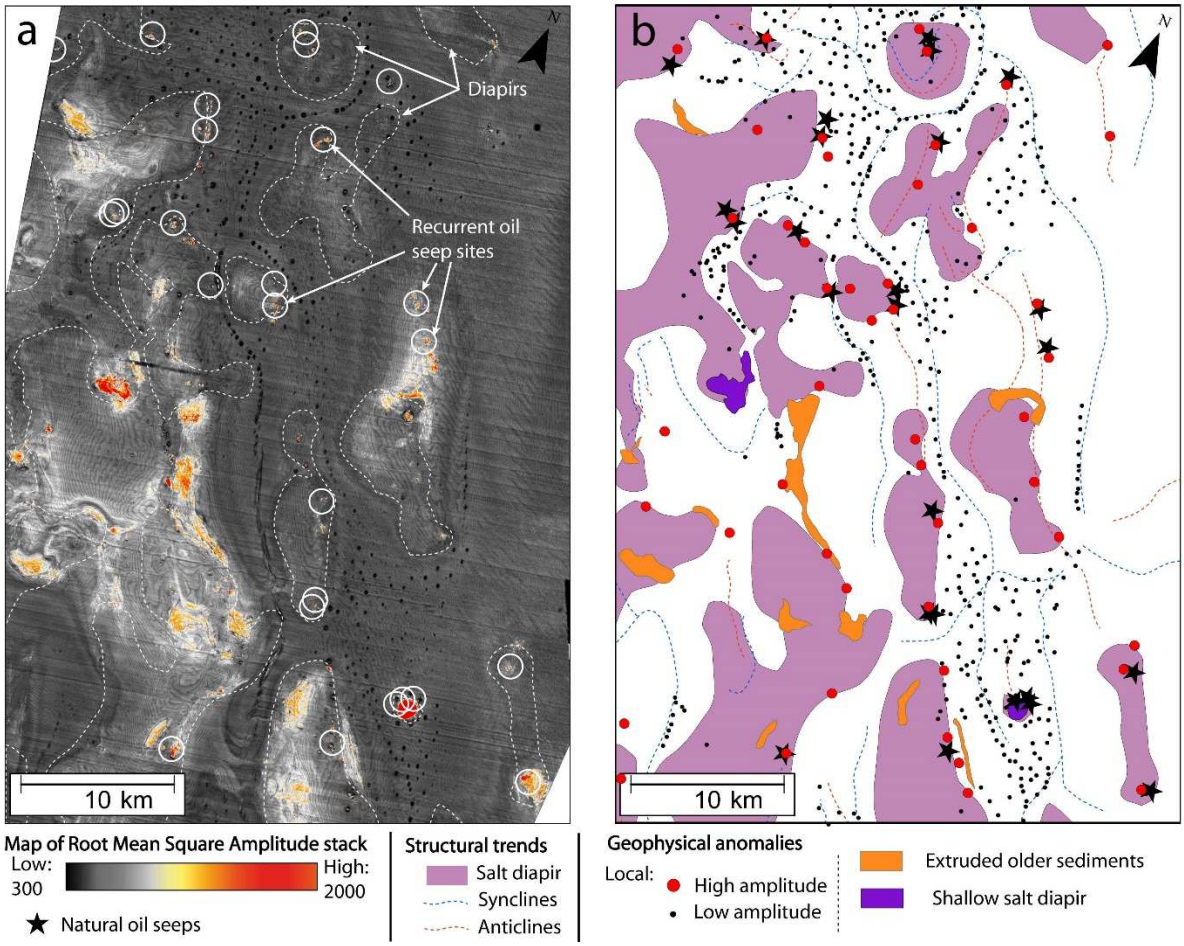

420

421 **Fig. 9: a. Map of the RMS amplitude stack of the first 100 ms TWT below seafloor. Geophysical**
422 **positive amplitude anomalies are visible as warm colours. White circles show the average surfacing**
423 **areas of recurrent oil seeps. b. Map of the allochthonous salt represented as purple polygons. The**
424 **anticline/syncline of the Late/Early Pliocene transition is displayed as red and blue dashed polylines,**
425 **respectively. The geophysical anomalies extracted from the RMS amplitude stack are categorised**
426 **into four main families: shallow salt diapir, exhumed older and compacted sediments, pseudo-**
427 **circular amplitude diming and vertical stack of pseudo-circular high-amplitude anomalies.**

428 ### *4.3.2. Negative polarity reflections*

429 Occasionally, consistent negative reflections crosscut stratigraphic series with all the characteristics of
430 a methane hydrate BSR. The BSR occurs as extensive reflectors in minibasins with a distance from the
431 seafloor ranging roughly from 250 to 500 ms TWT and is usually underlain by a thick High-Reflectivity
432 Zone (***Andresen et al., 2011***).

433 Approaching the salt diapirs, the BSR shoals up to a range of 50 to 250 ms TWT below the seabed; it
434 generally occurs in discrete small patches (Fig. 10a). This difference between the overburden of the
435 diapirs and minibasins is known to be associated with the high thermal conductivity of the salt, which
436 concentrates heat above diapirs, resulting in a higher geothermal gradient there, and consequently a
437 thinner hydrate stability zone ***(Lucazeau et al., 2004***). The BSR corresponds to the basal limit of pipe-
438 like features (type 3 anomalies) characterised by a vertical succession of PHAA and is underlain by a
439 100 ms-thick high-amplitude interval.

440 The sub-surface series are also locally affected by an occasional second negative polarity reflection.
441 The horizon occurs as a continuous, crosscutting surface and tends to be parallel to the first BSR. The
442 vertical distance with the BSR is mostly constant (~50ms), or occasionally increases towards the
443 minibasins (Fig. 10). The thermal effect associated with the presence of a salt diapir also affects the
444 vertical location of the second BSR by decreasing the distance from the seafloor. Double BSRs are
445 observed exclusively above salt diapirs. Both BSRs are concomitantly and locally deflected upward
446 below seafloor depressions, which also correspond to the locations of PHAA (Fig. 10).

447

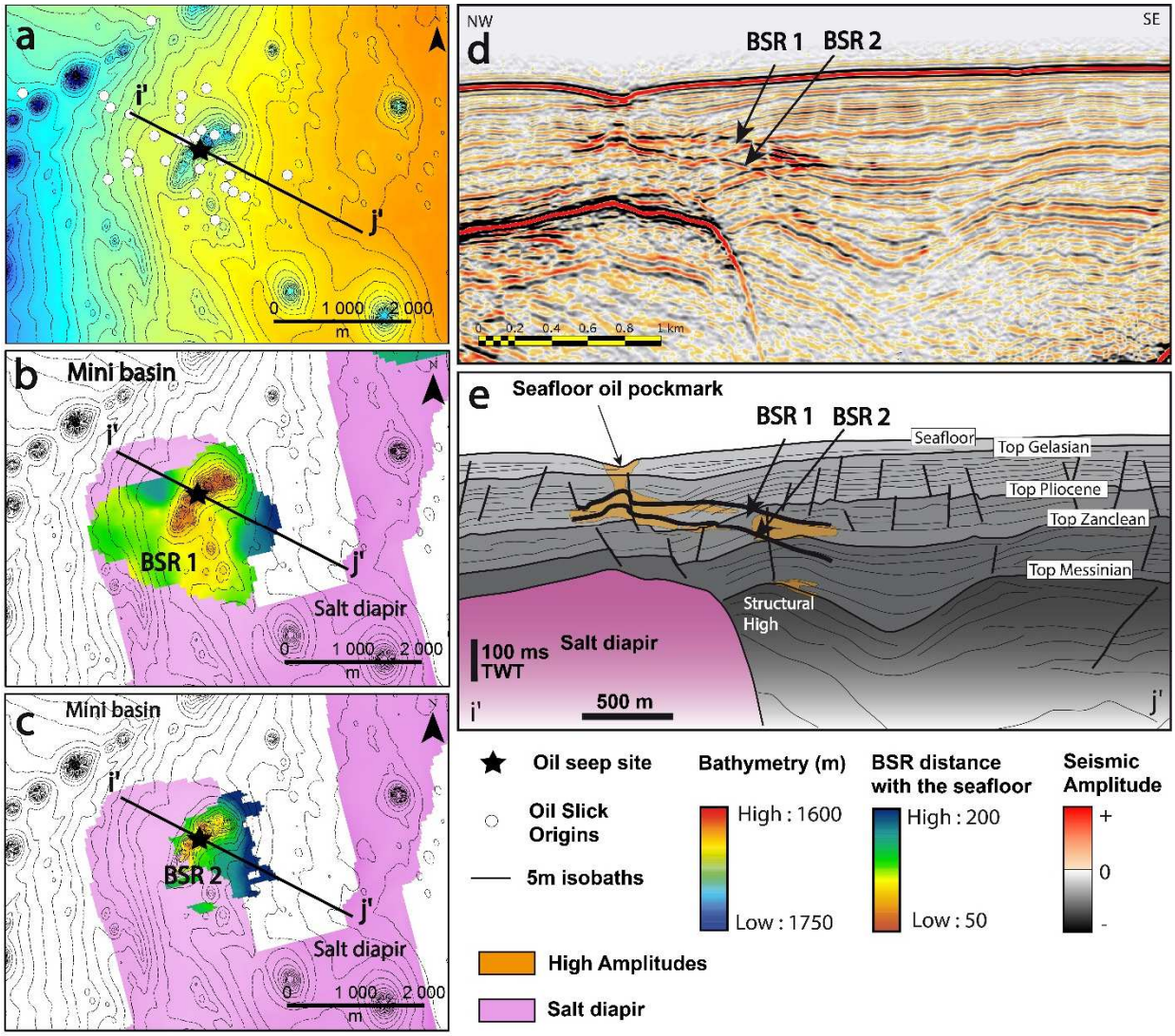

448

449 **Fig. 10: a. Seafloor map superimposed with 5m isobaths, oil slick origins (*OSO; Garcia-Pineda et al.,***
450 ***2010* and location of oil seeps identified with the SAR system. b. TWT difference map between upper**
451 **BSR and seafloor, superimposed with the extension of the underlying diapir and 5m isobaths. c. TWT**
452 **difference map of the lower BSR with the seafloor, superimposed with the underlying diapir**
453 **extension and 5m isobaths. d. Seismic section across a double BSR marked by two stacked black**
454 **horizons (see location in Fig. 10.a) e. Interpretative line drawing.**

455 ### *4.3.3. Subsurface high impedance layer*

456 A consistent High-Impedance Layer (HIL) frequently appears on sub-bottom profiler sections, in the
457 shallow sub-surface above the salt diapirs (Fig. 8 H). HIL are only identified on the high-resolution
458 survey and consist of a high-amplitude cross-cutting reflector. High-Impedance Layers occur in patches

whose surface areas can reach 120 km², the average being 20 km² (Fig. 11 b). They are located above diapiric areas, mostly at the upslope flank but can also be occasionally found downslope. The TWT difference with the seafloor ranges from 0 to 80 ms TWT above diapirs and can be higher (up to 200 ms TWT) in minibasins.

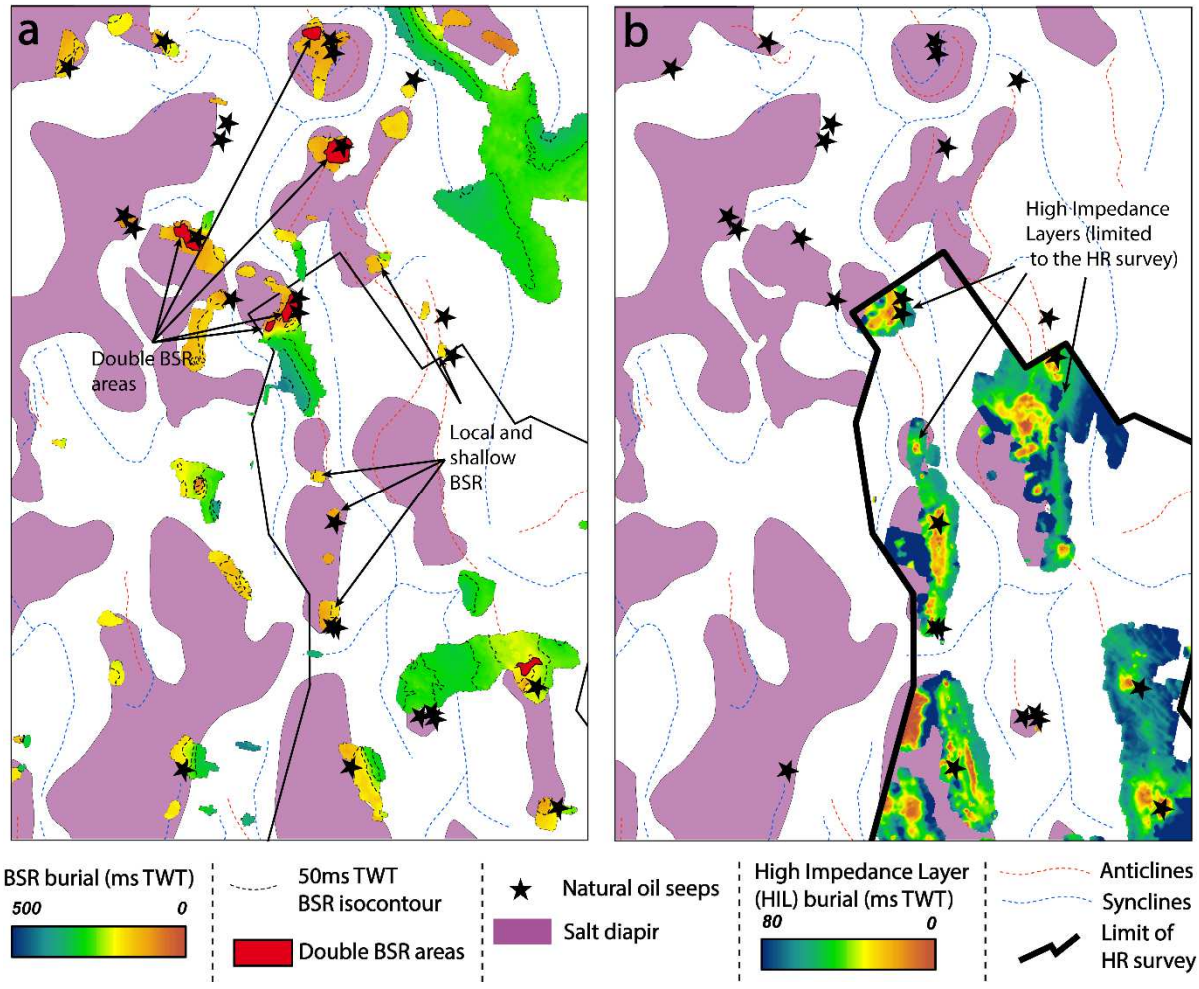

Fig. 11 : a. Extract of the Bottom Simulating Reflection (BSR) map with basin structure in background illustrating the relationship with hydrate and oil seep sites. b. Isochron map of the HIL in the shallow sub-surface from sub-bottom profiler data. The colour scale displays the distance between the seismic horizon and the seafloor.

5. Synthesis and discussion

5.1. Integrative synthesis of the oil seepage situation

A subset of 22 cores spatially corresponds to the vertical projection of recurrent oil seep sites detected from the SAR study, within a radius of < 1500 m (red dots and green triangles in Fig. 4b). Geochemical analyses were successfully performed for 19 out of 22 cores. For these sampled oil seep sites, the C_{15+} concentration (Sn Alkanes + UCM) shows high concentrations of heavy hydrocarbons and TSF values at least 50 times higher than the regional background. A large majority (17/19) of sampled oil seep sites fall into the "Probable" and "Sure" categories and the remaining (2/17) into the "Possible" category (red dots and green triangles in Fig. 4b). These observations validates the assumption that lateral drift in the water column averages to nil over time and confirms that, without any systematic offset, the pockmarks beneath the barycentre of OSOs corresponds to the source of expelled oils, on a regional scale as demonstrated from integration of vertical mooring data (***Jatiault et al., 2018***). Considering that 58 pistons belong to the "Probable" and "Sure" categories, 38% (22/58) correspond to the location of recurrent seepage slicks detected with the SAR system. The oil gravity, estimated using the fluorescence technique, ranges from 10 to 40°API for active oil seep sites associated with sea surface manifestations of oil.

Even though visual confirmation of asphalt inclusion remains uncommon (10 cores; black triangles in Fig. 4a), 40% of drilled sites showing asphalt inclusions (4/10; green triangles in Fig. 4b) are located close to a recurrent seep site at the sea surface. The geochemical analysis is available for 2 cores associated with asphalt inclusions and shows that the TSF values and the concentration in C_{15+} reaches the highest values in the core dataset (Fig. 4b).

We identified multiple fluid-related morphotypes on the seafloor in our study area (Fig. 5). Let us examine which ones can be considered characteristic of oil-bearing seeps compared to other fluid releases, by comparing geophysical features against the results of the SAR study. The number of conical pockmarks, including aligned and isolated cones, represents 85% of the total fluid escape features

identified on the bathymetric data (1 750 individual features) (Table 3). Although these features are abundant, none are presently responsible for oil seepage detected with SAR systems. Conversely, clusters of heterometric pockmarks, irregular pockmarks and submarine mounds are occasional across the margin. Respectively, 109, 175 and 17 were indexed from bathymetric analyses, making barely 15 percent of the total number of identified seafloor fluid-escape features. These 15 percent account for 98% of seafloor vents responsible for oil supply during the observation period (Table 3).

Seafloor hummocky areas are associated with oil slicks detected with SAR data for 5 out of the 10 seafloor hummocky areas detected on the HR dataset and 21 out of the 50 identified from the 3D seismic. Both the HR survey and information deduced from 3D seismic suggest that barely half of asphalt mounds fields are associated with detectable and recurrent slicks at the sea surface (21 out of entire 50 hummocky areas array).

On the subsurface, the area imaged with the 3D seismic covers 30 individual recurrent oil seep sites, 28 of which are either directly related to shallow salt diapirs, or correspond to the outcropping older sediment slabs uplifted by differential salt movements. The seafloor origin of recurrent oil seep sites visible exclusively on SAR data (100 %) corresponds to PHAA pipes in the shallow subsurface (<100ms; Fig. 9). Among the 75 individual vertical pipes identified (type 3; Fig. 8 A), about 40% of geophysical anomalies (30/75) are currently associated with prolific seep sites. Conversely, none (0%) of low amplitude pipes identified across the study area are associated with oil seeps visible on space-borne data. Among the 75 local positive geophysical anomalies (type 3) recognised using the 3D seismic, about 60 % (45/75) are associated with a BSR. Among the 30 recurrent oil seep sites imaged with 3D seismic, 21 (70 %) are emplaced directly above a shallow BSR. Double BSR are unusual in the study area but exclusively occur to oil seep sites detected with the SAR system (see red patches in Fig. 11 a). Six of the 30 recurrent oil seep sites detected with the SAR system and imaged with 3D seismic are directly emplaced above a double BSR. All the detected oil seeps belong to the areas associated with the development of a HIL (Fig. 11 b). Moreover, the interpreted seafloor origin of oil seeps (irregular isolated pockmarks and cluster of heterometric pockmarks; Fig. 5) corresponds to areas where the HIL

reach the seafloor. There is a strong geographical correlation between seafloor-reaching HIL, shallow local BSR and PHAA. At the submarine mound locations, the interface between the series affected by and unaffected by the HIL are characterised by a sharp, strong acoustic impedance contrast (Fig. 5d). The HIL crosscuts the stratigraphic series and rise towards the seafloor at the mound locations without revealing any particular internal organisation compared to stratigraphic boundaries. At the location of complex shaped pockmarks, the interface between the series affected and unaffected by the HIL is continuous and sometimes tends to align with stratigraphic boundaries (Fig. 5e).

Table 3 : Synthesis of fluid flow manifestations as observed throughout the study area compared to detectable oil seeps. Pockmarks inventory are deduced from the interpretation of the 12.5m resolution multi-beam bathymetry. Coupling the features related to oil seep sites with non-seeping geophysical anomalies contributes to the understanding of the seepage potential.

Fluid flow manifestations		Total picked-out	Oil supplying sites (SAR data)	
			Active	Percentage of correlation
Submarine mounds		**17**	**6**	**30 %**
Complex shaped pockmarks	Cluster of heterometric pockmarks	**109**	**53**	**49 %**
	Irregular isolated pockmarks	**175**	**26**	**15 %**
Regular shaped pockmarks	Isolated conical pockmarks	**890**	**2**	**< 1%**
	Aligned conical pockmarks	**589**	**0**	**0 %**
Total picked-up		**1750**	**87**	**/**
Seafloor asphalt mounds	HR bathymetry (3m)	**10**	**5**	**50%**
	3D bathymetry (12.5m)	**50**	**21**	**42 %**
Seafloor geochemical coring (<1500 m)	"Probable" and "Sure" categories	**58**	**22**	**38 %**
	Visual asphalt inclusion	**10**	**4**	**40 %**
Geophysical anomalies (n°3)	From 0 to 100 ms TWT	**75**	**30**	**40 %**

5.2. Significance of thermogenic seep sites geometry

5.2.1. Seafloor expressions

Defining characteristic features of thermogenic seeps on geophysical data is crucial for the understanding of petroleum system plays, to define the best seafloor coring targets and to seek and inventory extreme marine ecosystems (***Jones et al., 2014***). As demonstrated by previous studies on the LCB (***Andresen, 2012; Jatiault et al., 2019, Part I***), the location of seafloor thermogenic seeps is controlled by the shallow deformation related to the salt tectonics. Thermogenic pockmarks locate along faults associated with the underlying diapir deformation. Therefore, the location of seafloor seeps, especially clusters of heterometric pockmarks is consistently influenced by the underlying salt tectonics-related fault network. Both clustered and irregular pockmarks occur above fluid-related seismic anomalies, such as high-amplitude vertical pipes (***Løseth et al., 2011***), shallow HIL, BSR(s), or above salt. The distinction between clustered and irregular pockmarks is facilitated using the HR bathymetry, while the characteristics of the subsurface are similar. The distinction between the two is sometimes tricky and can be subject to data resolution issues or could mark a temporal evolution that depends on seepage persistence over time. The geometrical distinction could correspond to the process evolution, one being the initial stage of the other. In actively deforming areas above salt, the area affected by seepage features is likely to correspond to areas undergoing active fracturing; the pinpoint versus distributed character of seeps may reflect the localised versus distributed character of fracturing.

Previous work on the LCB reported a large number of clustered pockmarks at roughly 550 metres depth (***Gay et al., 2007***), i.e. along the feather edge of the BSR at the seabed. The presence of salt is known to deform the temperature field above and around diapirs (***Lucazeau et al., 2004***), and may affect the salinity of formation water conditions. However, the identification of BSRs above salt diapirs in this area indicates that the BGHSZ remains within the sedimentary interval at salt protrusion areas (Fig. 11). The strict association between submarine mounds and spiky diapirs suggests that the development of mounds depends on the degree of focusing of the hydrocarbon migration system.

557 Similar shaped submarine mounds (Pingoes) were described and interpreted as composed of
558 carbonate reefs interspersed with hydrates patches in the Norwegian Sea (***Hovland and Svensen,***
559 ***2006***), but also in the Kwanza basin interpreted as imprinting the development of underlying hydrates
560 nodules (***Serié et al., 2012***).

561 Studies conducted at the salt front of the LCB led to differentiating active from inactive sites based on
562 seafloor reflectivity strength (***Wenau et al., 2014***), applying the general criterion defined by ***Sager et***
563 ***al. (2003)*** who relate low backscatter area to dormant sites. In our study, we observed major recurrent
564 oil seeps on SAR data that are associated with a "moderate" seafloor response (Fig. 3 in ***Wenau et al.,***
565 ***2014***).

566 Authigenic carbonate precipitation is presumed to consume methane in priority (Anaerobic Oxidation
567 of Methane; e.g. ***Barnes and Goldberg, 1976; Ivanov et al., 1989; Boetius et al., 2000; Paull and Ussler,***
568 ***2008; Knittel and Boetius, 2009; Boetius and Wenzhöfer, 2013***). The seafloor reflectivity strength used
569 in this study is rather similar between oil-supplying and non-oil-supplying seeps (Fig. 5), even if slope
570 artefacts may occur. Recent studies have shown that the type of carbonates is different between
571 systems dominated by oil and gas (e.g. ***Hudson, 1997; Thomas et al., 2011***; ***Smrza et al., 2016***), which
572 might involve a difference in precipitation rate.

573 Pockmarks associated with pore-water and biogenic methane release occur extensively in minibasins
574 in relation to local-scale features such as polygonal faults (***Andresen and Huuse, 2011; Maia et al.,***
575 ***2016***) and/or tectonic faults (***Gay et al., 2006 c***). Methanogenic carbonate precipitates even in the case
576 of a "slow seep" (***Ho et al., 2012)***. The absence of positive high-amplitude anomalies (***Ho et al., 2012***)
577 in association with conical pockmarks therefore suggests that the associated fluid is likely pore-water
578 dominated. We have observed that pockmarks located in minibasins are steeper (~15°) and more
579 conformable compared to those located above diapirs. Let us examine the factors that could explain
580 this difference. The mid Plio-Quaternary sedimentation in salt minibasins is dominated by fine-grained
581 sediments that act as an impermeable barrier to fluid migration (***Uenzelmann-Neben, 1998; Anka et***

al., 2013). The sediment type could have a strong influence on pockmark geometry; the recent sedimentary overburden being gently eroded across the fluid ascent path could explain the conformable geometry of minibasin pockmarks. The uplift of older/coarser Miocene/Mid-Pliocene sediments (***Anderson et al., 2000***), combined with salt-induced faulting and seafloor hydrates/carbonates distribution might be good candidates to generate multiple seafloor fluid outlets (***Jatiault et al., 2019***). In this condition, this could explain the morphological differences between thermogenic seep sites above diapirs and pore-dewatering escape features in minibasin.

5.2.2. Sub-seafloor expression

Oil-supplying seeps correspond to small (100m diameter) sub-circular high amplitude anomalies on the seafloor amplitude map (d, e and f in Fig. 5; n°3 in Fig. 8A). The presence of a BSR shows that migration is focused above diapirs and that the presence of anomalies above the base of the hydrates indicates that the hydrate seal is locally breached when the fluid overpressure is too high (***Cathles et al., 2010***). The vertical successions of strong reflections are interpreted as fluid escape pipes (Fig. 8 G; ***Löseth et al., 2011; Karstens et al., 2015***) which can be related either to vertical stacking of authigenic carbonate cementations or pavements (***Hovland et al., 1987; Hovland, 2002; Pierre and Fouquet, 2007; Römer et al., 2014***), vein-filled/ hydrate-rich sediments (***Sahling et al., 2008***) or gas-charged sediments (***Schroot et al., 2003***).

Outcrops of Miocene-Pliocene sediments at the seabed are privileged leakage pathways due to changes in lithologic properties from fine-grained/high cap-rock efficient upper Pliocene and Quaternary silts and clays to coarser, more permeable Miocene series (***Anderson et al., 2000***) and appear as privileged fluid outlets.

The negative impedance contrast resulting in the BSR is known to primarily reflect the presence of free gas beneath the base of the hydrates stability zone, rather than the increase of impedance due to the presence of hydrates above (***Holbrook, 2001***). The identification of a second BSR was reported in a few case studies (***Andreassen et al., 2000; Foucher et al., 2002; Popescu et al., 2006; Posewang and Mienert, 1999; Zander et al., 2017***) with various interpretations (changes in environmental conditions,

608 paleo BSR relics, and heavier gas components). In the LCB, the observations of a second cross-cutting
609 and negative polarity reflections exclusively occur; (1) at the crest of salt diapirs and (2) in the
610 conditions of proven thermogenic fluid seepage from the identification of recurrent slicks. The second
611 BSR could be associated with heavier gas components in conditions of abundant thermogenic
612 dysmigration ***(Jatiault et al., 2019, Part I)***. Stacked BSR 1 and 2 would then involve distinct hydrocarbon
613 compositions between the two layers, which excludes the hypothesis of a mix of hydrocarbon
614 components from BSR1 and BSR2, and therefore suggests distinct migration pathways. In that case,
615 the 100% methane-related BSR would probably follow a lateral path along minibasin stratigraphic
616 interfaces towards the crest of the diapir. Knowing that structure II and H hydrates are stable are
617 greater depths (***Sloan, 1990***) and considering the limited extent of BSR2, the thermogenic BSRs would
618 follow more vertical advection paths along salt flanks.

619 ## 5.3. Relevance of multi-scale integrated evaluation of the thermogenic
620 ## seepage potential

621 ### *5.3.1. Pre-existing methodology*

622 The combination of different geophysical observations provides key features to better understand
623 hydrocarbons seep systems and fluid flow phenomena (***Serié et al., 2017***). The integration of multi-
624 proxy tools is relevant for confirming source rock maturation and for studying fluid migration across
625 sedimentary series. The technique used in pre-existing methodology has its own advantages and
626 limitations that are listed and explained below:

627 - For underexplored areas, remote sensing analysis provides a first-order approach for
628 evaluating the seepage potential (***Williams and Lawrence, 2002***). The main SAR system limitations are
629 its limited spatial resolution (Table 1) and dependency on weather conditions (1.5 to 5.5 $m.s^{-1}$; ***Jatiault***
630 ***et al., 2017***). On SAR images, low backscatter areas can also be look-alikes (such as algae blooms,
631 surface micro-layer; ***Mityagina et al., 2007***) and the natural origin of low radiometric features without
632 a seafloor validation therefore remains questionable, even when recurrent (***Ryan et al., 2010***). The

633 SAR detectability thickness threshold may prevent the recognition of active oil seeps when the oil flow
634 is low.

635 - Even low-intensity oil seep sites are detectable with seabed geochemistry using fluorescence
636 analysis (***Abrams, 2005***). The recognition of asphalt inclusions in cores demonstrates the thermogenic
637 origin of fluid migrations. However, the pinpoint nature of geochemical coring means that even with a
638 dense set of cores, the technique potentially misses a large array of active seep sites.

639 - The seafloor seismic amplitude provides information on lithological modifications, especially
640 above salt diapir where the outcropping Pliocene/Miocene series constitutes privileged pathways for
641 migrating fluids.

642 - The identification of a negative polarity BSR also helped us locate focused hydrocarbon fluid
643 migration above salt diapirs (***Taylor et al., 2000; Lucazeau et al., 2004; Serié et al., 2017***). In the
644 context of a shallow underlying diapir, the associated thermal anomaly creates an upward
645 displacement of the BSR that is suitable for the formation of a hydrate-related trap for hydrocarbon
646 migration. However, the survival period of a BSR following the cessation of fluid migration remains
647 under-documented, limiting the appraisal of seepage activity.

648 ### *5.3.2. Improvements of the methods*

649 In addition to pre-existing methodology, the following additional data analysis can help to refine the
650 fluid flow phenomena in sedimentary basin (Fig. 12). Let us examine what are the improvements
651 performed by the integration of additional data:

652 - A detailed analysis of surface slicks better constrains oil seep sites locations and address the
653 present-day seepage expelled volumes. In this study, recurrent surface slicks were successfully linked
654 with seafloor features 98% of the time. This confirms the relevance of combining the SAR system with
655 marine geophysical surface data to constrain hydrocarbon plumbing system during the exploration
656 workflow. The occurrence rates defined as the ratio between the amount of detected slicks and SAR
657 data coverage range from 5 to 80% (***Jatiault et al., 2017***). Considering that the SAR system efficiency

depends on weather conditions and that active seep sites are mostly intermittent, exhaustive inventory of oil seep sites relies on a high multi-temporal satellite data coverage with at least fifty overlapping SAR scenes in our study area. The amount of oil that naturally enters the marine environment is roughly split into two equal parts between natural seepage and human activity (***Prince et al., 2003***). For quantitative geological studies, it is necessary to discriminate natural seepage to unnatural oil (***Macdonald et al., 2015***). Considering average displacement values at the sea surface in the LCB of 17 $cm.s^{-1}$ due to surface currents and winds (***Jatiault et al., 2017***) and assuming that slicks thinner than 0.1 µm thick are not detectable (***de Beukelear et al., 2003***), the estimated minimum detectable oil flow varies between 0.76 to 9.2 $l.h^{-1}$ depending on the spatial resolution of SAR systems (Table 4). Considering that 4380m^3 are expelled annually from one hundred seep sites (***Jatiault et al., 2017***), the average expelled volume of a random oil seep is estimated at 5 $l.h^{-1}$ in the study area. This demonstrates that the expelled volume is within the order of the detectability threshold. The SAR detectability thickness threshold might therefore be too high to detect the activity of a subset of potential seep sites interpreted from seismic data.

Table 4 : Minimum oil output estimation depending on the spatial resolution of different SAR systems.

Satellite/ Sensor	Envisat /WSM	ERS/IMP	Cosmo-SkyMed	TerraSAR – X	RADARSAT-2
Pixel Spacing (m)	75	12.5	3-15	20	25-50
Minimum volume output ($l.h^{-1}$)	9.2	0.76	0.18 – 0.92	1.22	3.06 – 6.13

- The integration of current profilers (or the use of regional metocean models when the former are not available) helps constrain probable oil migration routes through the water column and quantify the probable lateral deflection (***Jatiault et al., 2018***).

- The detection of asphalt mounds on HR survey confirms that oil is migrating towards the seafloor and constitutes another proof of an active oil-seep sites (***Jones et al., 2014***). The presence of asphalt mounds implies that hydrocarbon dysmigration is sufficiently slow for the oil to be heavily degraded and stored on the seafloor (***Head et al., 2003; Larter et al., 2003; Jones et al., 2008; Larter***

681 ***et al., 2006; Peters et al., 2005; Peters et al., 2007; Jones et al., 2008***). In the present case, using
682 specific seismic attributes such as curvature identified a high proportion of the mounds and may be
683 used at least for a first screening.

684 - The computation of an RMS amplitude map of shallow subsurface (first 100 ms in this study)
685 quickly pinpointing isolated sub-circular high-amplitude anomalies likely to sign the presence of fluid
686 migration, while reducing the amplitude anomaly associated with the slope inflection. Vertical stacking
687 of anomalies, if observed on cross-sections, is a strong additional indication of hydrocarbon leakage.
688 However, the technique is irrelevant for assessing the fluid type.

689 - We observed double BSRs only at the location of oil seeps proven by SAR analysis. Double
690 BSR could mark the basal level of stability of a mix of heavier gas. Additional studies would be needed
691 to know if this is related to compositional or concentration effects.

692 - The HIL is presumably related to limited-size carbonate slabs with shallow asphalt and
693 potentially with hydrates (***Jatiault et al., 2019, Part I***) also helps locate active hydrocarbon seepage.
694 HIL patches are typically wide, but reach the seabed in a very limited area; consequently, the
695 identification of the point where the HIL reaches the seabed reduces the uncertainty on the
696 identification of the point of seepage. The SBP dataset provide information on sub-seafloor hardness
697 and possibly a discrimination between similar shaped features, i.e. soft mud volcanoes (***Serié et al.,***
698 ***2017***) compared to harder carbonate and/or hydrate mounds/pingoes (this study; ***Hovland and***
699 ***Svensen, 2006***). The proximity of HIL features with the seafloor also constrains seep outlets location
700 and improve the targeting of cores locations. However, the deployment of such toolsets in a given area
701 implies that the given area has already been extensively explored.

702 The combination of different observations and techniques provides an integrated vision of the
703 hydrocarbon fluid seepage phenomena in the Lower Congo Basin and helped refining the methodology
704 of studying the fluid flow phenomena (Fig. 12).

705

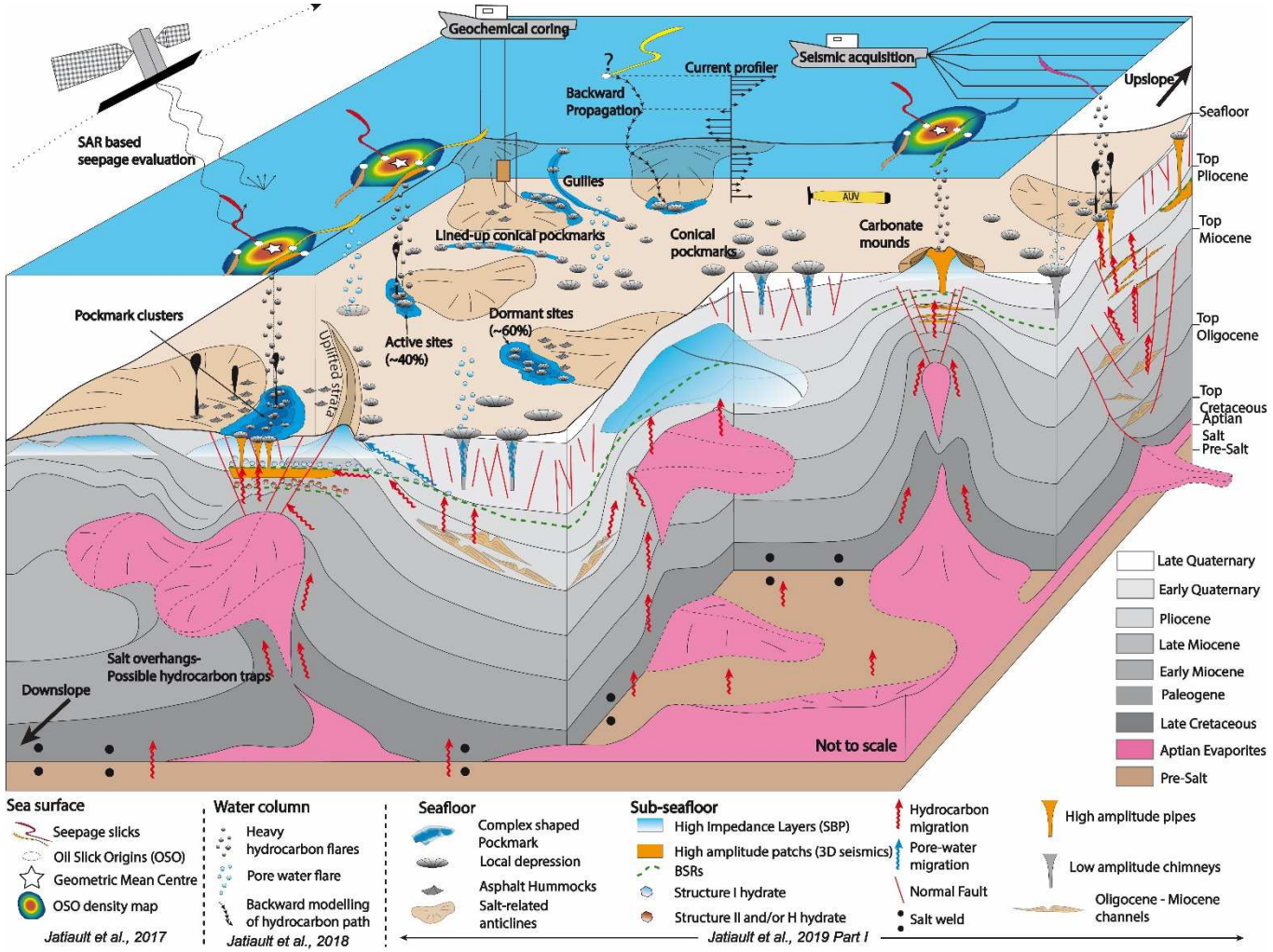

706

707 **Fig. 12: Synthetic block diagram illustrating the methodology and the main results concerning the characterization of the heavy hydrocarbon fluid flow in**

708 **the Lower Congo Basin.**

709 The inventory of geophysical features associated with the oil seeps sites in this study would benefit
710 from comparative studies conducted in different geological contexts.

711 5.4. Spatio-temporal variability of oil seepage activity

712 The combined manifestation of recurrent sea-surface slicks and seafloor evidence of active fluid flow
713 demonstrates that liquid hydrocarbons are currently being expelled from the seafloor in the study
714 area. The combination of seismic data together with SAR imagery and geochemical features validated
715 the natural origin of the seepage (***Serié et al., 2017***). We highlighted a series of geophysical features
716 (seafloor and subsurface) associated with oil-seep systems that were extrapolated towards similar fluid
717 flow features that could also be responsible for thermogenic escapes, namely potential oil-seep sites.
718 Both geochemical and geophysical evidence demonstrate that many potential seep sites were not
719 associated with recurrent sea-surface slicks. The present-day seepage activity observed on SAR data
720 corresponds to 40 % of the total array of potential oil seep sites detected on the seafloor and sub-
721 surface (Table 3). The remaining 60 % of geophysical anomalies n°3 present the same characteristics
722 as active oil seep sites and most of them (75 %) are overlain by a seafloor fluid-flow feature, which
723 shows that most are active at seismic resolution scale and suggest much longer emission frequencies.

724 The active array proportion is concordant with results published in the Gulf of Mexico, where 50% of
725 geophysical anomalies identified on seismic datasets correspond to an active oil seep site at the sea
726 surface (***Garcia-Pineda et al., 2010***). Oil seep sites are mostly transient with a widespread range of
727 periods of recurrence (***Garcia-Pineda et al., 2010; Garcia-Pineda et al., 2015; Jatiault et al., 2017***).
728 The SAR data collection dates from 1994 to 2016, which is very brief in comparison to geological time
729 scales. The remaining 60% of geophysical anomalies could also be associated with dormant seep sites
730 whose inactive stages: (1) exceed the SAR monitoring period (22 years), or (2) are shorter than SAR
731 acquisition intervals (varying from few hours to few months).

732 Barely half of seafloor areas characterised by seafloor asphalt presence (seafloor mounds and oil-
733 impregnated cores) are currently supplying oil. Using fluorescence as a proxy for oil gravity (***Abrams,***

734 ***2005***), seafloor samples in our study area range from 10 to 40°API. High biodegradation leads to an
735 increase in the density of the oil in the reservoirs (***Head et al., 2003; Peters et al., 2007***) but also in the
736 shallow sub-surface (e.g. ***Zengler et al., 1999; Wilkes et al., 2001***), so that biodegraded oils can reach
737 density values greater than that of ocean water (***Larter et al., 2003***). For oil when the °API gravity is
738 below that of ocean water (10), asphalts remain stored on the seafloor (***Macdonald et al., 2004; Jones***
739 ***et al., 2014***). Bathymetric hummocky features, reportedly composed of a large volume of stored
740 asphalt on the seafloor, have already been observed in other provinces without sea surface
741 manifestations (***Keller et al., 2007; Valentine et al., 2010***).

742 Extreme marine ecosystems are highly reactive to hydrocarbon flow fluctuations with a survival period
743 following seepage extinction of about one year (***Hessler et al., 1988; Shanks, 1995; Shank et al., 1998;***
744 ***Mullineaux et al., 2000***). In-situ records of photo/video from ROV dives would greatly help ascertain
745 the presence of modern chemosynthetic communities and therefore address the seeping mechanism
746 and activity of the remaining 60% dormant geophysical anomalies (***Charlou et al., 2004, Gay et al.,***
747 ***2006a, Marcon et al., 2014***).

748 Comparable studies conducted in similar geological context, yet revealed a much tenuous oil seepage
749 manifestations (***Serié et al., 2017***). Recent sedimentation stage of the LCB were particularly high due
750 to the establishment of the Congo DSF during Neogene and upwelling system during Early Quaternary
751 (***Savoye et al., 2000; Ferry et al., 2004; Seranne and Anka, 2005; Marcano et al., 2013***), which lead to
752 salt-related deformation enhancement. The tectonic regime of seeping provinces, mostly transitional
753 in Kwanza basin and compressive in LCB could play a significant role on expelled volumes.

754 6. Summary and Conclusions

755 We used several tools to assess the seepage potential in the distal salt province of the Lower Congo
756 Basin. The analysis of sea-surface oil manifestations imaged with satellite imagery, coupled with a
757 dense geochemical core-set and seafloor/ sub-seafloor manifestations of oil presence provides an
758 integrated approach of the present-day seepage efficiency.

- The geophysical features of thermogenic seeps sites previously recognised at local scale (***Jatiault et al., 2019, Part I***) are validated at the full scale of the study area. Thermogenic seeps sites (1) consist of complex-shaped features (clusters of irregular pockmarks and seafloor mounds), (2) are associated with shallow high-impedance layers on the sub-bottom profiler and (3) are underlain by BSR that (4) are underlain by consistent amplitude and (5) are overlain by clusters of pipe-like features (PHAA).
- The knowledge of the fluid flow phenomena is improved from the integration of detailed slicks map that provide a means to quantify seepage activity. The SBP data that provides a discrimination technique between hydrocarbons and pore dewatering features and also reveals the seafloor distribution of asphalt storage areas.
- About 40% of geophysical anomalies are associated with recurrent oil slicks at the sea surface while the remaining 60% are most likely related to dormant seep sites whose periodicity exceeds the 22-year SAR monitoring or are shorter than SAR scene acquisition intervals.
- A large number of low-amplitude pipes (582) were identified in salt minibasins from the 12.5m seismic resolution that are linked with conical-shaped seafloor pockmarks, interpreted as related to pore-water expulsion.
- Extensive high amplitudes related to the uplift of older/coarser/ more permeable sediments due to the salt tectonics and characterised by extensive near-surface positive amplitude geophysical anomalies appear to correspond to preferential seafloor thermogenic migration outlets.
- Only 20% of BSRs are double, and these occur exclusively in association with thermogenic hydrocarbons seeps.

Acknowledgements

The authors express their grateful thanks to Total SA, Total Angola (TEPA) and partners for the data disclosure approval of the industrial seismic and sub-bottom profiler data. The authors thank Total

team DSO for the geochemical analysis. This work was performed in the frame of a PhD project (CIFRE convention) granted by the ANRT (Agence Nationale de la Recherche et de la Technologie, No. 2014/0308), funded by Total SA in collaboration with University of Perpignan, France. The authors thank the European Space Agency (Envisat WSM, IMP) for the delivering of free-access data. Seismic interpretation was carried out using Total's proprietary software Sismage. We kindly thank Christophe Serié and an additional reviewer who provided critical suggestions in order to improve the impact and benefits of the paper.

References

Abrams, M.A. (2005). Significant of hydrocarbon seepage relative to petroleum generation and entrapment, Marine and Petroleum Geology 22, p. 457-477.

Anderson, J. E., Cartwright, J., Drysdall, S. J., & Vivian, N. (2000). Controls on turbidite sand deposition during gravity-driven extension of a passive margin: examples from Miocene sediments in Block 4, Angola. Marine and Petroleum Geology, 17(10), 1165-1203.

Andreassen, K., Mienert, J., Bryn, P., & Singh, S. C. (2000). A double gas-hydrate related bottom simulating reflector at the Norwegian continental margin. Annals of the New York Academy of Sciences, 912(1), 126-135.

Andresen, K. J., Huuse, M., Schodt, N. H., Clausen, L. F., & Seidler, L. (2011). Hydrocarbon plumbing systems of salt minibasins offshore Angola revealed by three-dimensional seismic analysis. AAPG bulletin, 95(6), 1039-1065.

Andresen K.J., & Huuse, M. (2011). 'Bulls-eye' and polygonal faulting in the Lower Congo Basin: Relative timing and implications for fluid expulsion during shallow burial, Marine Geology 279, 111-127, http://dx.doi.org/ 10.1016/j.margeo.2010.10.016.

806 Andresen, K.J. (2012). Fluid flow features in hydrocarbon plumbing systems: What do they tell us about
807 the basin evolution, *Marine Geology, 332-334*, 89-108,
808 http://dx.doi.org/10.1016/j.margeo.2012.07.006.

809 Anka, Z., Berndt, C., Gay, A., (2012). Hydrocarbon leakage trough focused fluid flow systems in
810 continental margins, Marine Geology p 332-334.

811 Anka, Z., Ondrak, R., Kowitz, A., Schodt, N. (2013). Identification and numerical modeling of
812 hydrocarbon leakage in the Lower Congo Basin: Implications on the genesis ok km-wide seafloor
813 mounded structures, *Tectonophysics, 604*, 153-171, http://dx.doi.org/10.1016/j.tecto.2012.11.020.

814 Anka, Z., Séranne, M., Lopez, M., Scheck-Wenderoth, M., & Savoye, B. (2009). The long-term evolution
815 of the Congo deep-sea fan: A basin-wide view of the interaction between a giant submarine fan and a
816 mature passive margin (ZaiAngo project), Tectonophysics 470, 42-56, http://dx.doi.org/
817 10.1016/j.tecto.2008.04.009.

818 Barnes, R. O., & Goldberg, E.D. (1976). Methane production and consumption in anoxic marine
819 sediments. Geology 4:297–300.

820 Barwise, T., & Hay, S. (1996). Predicting oil properties from core fluorescence.

821 Berndt, C., Bünz, S., Clayton, T., Mienert, J., & Saunders, M. (2004). Seismic character of bottom
822 simulating reflectors: examples from the mid-Norwegian margin. *Marine and Petroleum*
823 *Geology*, *21*(6), 723-733.

824 Boetius, A., Ravenschlag, K., Schubert, C. J., Rickert, D., Widdel, F., Gieseke, A., ... & Pfannkuche, O.
825 (2000). A marine microbial consortium apparently mediating anaerobic oxidation of methane. Nature,
826 407(6804), 623-626.

827 Boetius, A., & Wenzhöfer, F. (2013). Seafloor oxygen consumption fuelled by methane from cold seeps.
828 Nature Geoscience, 6(9), 725-734.

829 Brice, S.E., Cochran, M.D., Pardo, G., & Edwards, A.D. (1982). Tectonics and sedimentation of the South
830 Atlantic Rift Sequence: Cabinda, Angola. American Association Petroleum Geologists Memoir, 34, 5–
831 18.

832 Brownfield, M.E., & Charpentier, R.R. (2006). Geology and total petroleum systems of the west-central
833 coastal province (7203), west Africa (No. 2207-B).

834 Bünz, S., Mienert, J., Bryn, P., & Berg, K. (2005), Fluid flow impact on slope failure from 3D seismic data:
835 a case study in the Storegga Slide. Basin Research, 17(1), 109-122.

836 Burwood, R., (1999). Angola: source rock control for Lower Congo Coastal and Kwanza Basin petroleum
837 systems, Geological Society, London, Special Publications v. 152, p181-184.

838 Carruthers, D., Cartwright, J., Jackson, M. P., Schutjens, P. (2013). Origin and timing of layer-bound
839 radial faulting around North Sea salt stocks: New insights into the evolving stress state around rising
840 diapirs. Marine and Petroleum Geology, 48, 130-148.

841 Cartwright, J., Huuse, M., & Aplin, A. (2007). Seal bypass systems. *AAPG bulletin*, *91*(8), 1141-1166.

842 Cathles, L. M., Su, Z., & Chen, D. (2010). The physics of gas chimney and pockmark formation, with
843 implications for assessment of seafloor hazards and gas sequestration. Marine and petroleum Geology,
844 27(1), 82-91.

845 Charlou, J.L., Donval, J.P., Fouquet, Y., Ondreas, H., Knoery, J., Cochonat, P., Levaché, D., Poirier, Y.,
846 Jean-Baptiste, P., Fourré, E., Chazallon, B. (2004). Physical and chemical characterization of gas
847 hydrates and associated methane plumes in the Congo–Angola Basin *Chemical Geology, 205*, 405 –
848 425, http://dx.doi.org/10.1016/j.chemgeo.2003.12.033.

849 Cole, G. A., Requejo, A.G., Ormerod, D., Yu, Z., Clifford, A. (2000). Petroleum geochemical assessment
850 of the Lower Congo Basin, in Mello, M.R., and Katz, B.J., eds., Petroleum systems of South Atlantic
851 margins: AAPG Memoir 73, p.325-339.

852 Cunningham, R., & Lindholm, R. M. (2000). AAPG Memoir 73, Chapter 8: Seismic Evidence for
853 Widespread Gas Hydrate Formation, Offshore West Africa.

854 De Beukelear, S.M., MacDonald, I.R., Guinasso, N.L., Murray, J.A. (2003). Distinct side-scan sonar,
855 RADARSAT SAR, and acoustic profiler signatures of gas and oil seeps on the Gulf of Mexico slope*, Geo-*
856 *Marine Letters, 23*, 177-186.

857 Ferry, J. N., Babonneau, N., Mulder, T., Parize, O., & Raillard, S. (2004). Morphogenesis of Congo
858 submarine canyon and valley: implications about the theories of the canyons formation. Geodinamica
859 Acta, 17(4), 241-251.

860 Fort, X., Brun, J.P., & Chauvel, F. (2004). Salt tectonics on the Angolan margin, synsedimentary
861 deformation processes, AAPG Bulletin, 88:11, 1523–1544.

862 Foucher, J. P., Nouzé, H., & Henry, P. (2002). Observation and tentative interpretation of a double BSR
863 on the Nankai slope. Marine Geology, 187(1), 161-175.

864 Gade, M., Alpers, W. (1998). Imaging of biogenic and anthropogenic ocean surface films by the
865 multifrequency/ multipolarization SIR-C/X-SAR, *Journal of Geophysical Research, 103*, 18851-18866.

866 Garcia-Pineda, O., MacDonald, I., Zimmer, B., Shedd, B., Roberts, H. (2010). Remote-sensing evaluation
867 of geophysical anomaly sites in the outer continental slope, northern Gulf of Mexico, *Deep-Sea*
868 *research II 57*, 1859-1869, http://dx.doi.org/10.1016/j.dsr2.2010.05.005.

869 Garcia-Pineda, O., MacDonald, I., Silva, M., Shedd, W., Asl, S. D., Schumaker, B. (2015). Transience
870 and persistence of natural hydrocarbon seepage in Mississippi canyon, Gulf of Mexico. *Deep Sea*
871 *Research Part II: Topical Studies in Oceanography, 129*, 119-129.

872 Gay, A., Lopez, M., Berndt, C., Séranne, M. (2007). Geological controls on focused fluid flow
873 associated with seafloor seeps in the Lower Congo Basin*, Marine Geology 244,* 68 – 92,
874 http://dx.doi.org/10.1016/j.margeo.2007.06.003.

875 Gay, A., Lopez, M., Cochonat, P., Levaché, D., Sermondadaz, G., Seranne, M. (2006 a). Evidences of
876 early to late fluid migration from an upper Miocene turbiditic cannel revealed by 3D seismic coupled
877 to geochemical sampling within seafloor pockmarks, Lower Congo Basin, *Marine and Petroleum*
878 *geology 23, 387-399,* http://dx.doi.org/10.1016/j.marpetgeo.2006.02.004.

879 Gay, A., Lopez, M., Cochonat, P., Séranne, M., Levaché, D., Sermondadaz, G. (2006 b). Isolated
880 seafloor pockmarks linked to BSRs, fluid chimneys, polygonal faults and stacked Oligocene–
881 Miocene turbiditic paleochannels in the Lower Congo Basin, *Marine Geology 226*, 25 – 40,
882 http://dx.doi.org/10.1016/j.margeo.2005.09.018.

883 Gay, A., Lopez, M., Cochonat, P., Sultan, N., Cauquil, E., & Brigaud, F. (2003). Sinuous pockmark belt as
884 indicator of a shallow buried turbiditic channel on the lower slope of the Congo Basin, West African
885 Margin. In: Van Rensbergen, P., Hillis, R.R., Maltman, A.J., Morley, C.K., Subsurface Sediment
886 Mobilization, Geological Society of London, Special Publications, vol. 216, 173–189.

887 Gay, A., Lopez, M., Ondreas, H., Charlou, J.L., Sermondadaz, G., Cochonat, P. (2006 c). Seafloor facies
888 related to upward methane flux within a Giant Pockmark of the Lower Congo basin, Marine *Geology*
889 *226*, 81 – 95, http://dx.doi.org/10.1016/j.margeo.2005.09.011.

890 Guillon, S., & Keskes, N. (2004). Sismage and the 3d visualization at total. In AAPG International
891 Conference: October (pp. 24-27).

892 Haacke, R. R., Westbrook, G. K., & Hyndman, R. D. (2007). Gas hydrate, fluid flow and free gas:
893 Formation of the bottom-simulating reflector. Earth and Planetary Science Letters, 261(3), 407-420.

894 Haq, B. U., Hardenbol, J., & Vail, P. R. (1987). The new chronostratigraphic basis of Cenozoic and
895 Mesozoic sea level cycles. Timing and depositional history of eustatic sequences: constraints on seismic
896 stratigraphy: Cushman Foundation for Forminiferal Research, Special Publications, 24, 7-13.

897 Head, I. M., Jones, D. M., Larter, S. R. (2003). Biological activity in the deep subsurface and the
898 origin of heavy oil. *Nature, 426(6964)*, 344-352.

899 Heggland, R. (2002). Seismic evidence of vertical fluid migration through faults: applications of chimney
900 and fault detection. In *Proceedings from AAPG Hedburg Conference, Vancouver*.

901 Hessler, R. R., Smithey, W. M., Boudrias, M. A., Keller, C. H., Lutz, R. A., & Childress, J. J. (1988).
902 Temporal change in megafauna at the Rose Garden hydrothermal vent (Galapagos Rift; eastern
903 tropical Pacific). Deep Sea Research Part A. Oceanographic Research Papers, 35(10-11), 1681-1709.

904 Hill, A. J., Southgate, J. G., Fish, P. R., & Thomas, S. (2011). Deepwater Angola part I: Geohazard
905 mitigation. *Frontiers in Offshore Geotechnics II*, 209-214.

906 Ho, S., Cartwright, J.A., Imbert, P., (2012). Vertical evolution of fluid venting structures in relation to
907 gas flux, in the Neogene, Quaternary of the Lower Congo Bain, Offshore Angola.

908 Holbrook, W. S. (2001). Seismic studies of the Blake Ridge: Implications for hydrate distribution,
909 methane expulsion, and free gas dynamics. *Natural gas hydrates: Occurrence, distribution, and*
910 *detection*, 235-256.

911 Hovland, M. (2002). On the self-sealing nature of marine seeps. Continental Shelf Research, 22(16),
912 2387-2394.

913 Hovland, M., Heggland, R., De Vries, M.H., & Tjelta, T.I. (2010). Unit-pockmarks and their potential
914 significance for predicting fluid flow, Marine and Petroleum Geology 27, 1190 – 1199,
915 doi:10.1016/j.marpetgeo.2010.02.005.

916 Hovland, M., Jensen, S., & Fichler, C. (2012). Methane and minor oil macro-seep systems—their
917 complexity and environmental significance. *Marine Geology*, *332*, 163-173.

918 Hovland, M., & Judd, A. (1988). Seabed pockmarks and seepages: impact on geology, biology, and the
919 marine environment. Graham & Trotman Ltd., London, 293 pp.

920 Hovland, M., Talbot, M.R., Qvale, H., Olaussen, S., Assberg, L. (1987). Methane-related carbonate
921 cements in pockmarks of the North Sea, *Journal of Sedimentary Petrology, 57:5*, 881 - 892.

922 Hovland, M., & Svensen, H. (2006). Submarine pingoes: Indicators of shallow gas hydrates in a
923 pockmark at Nyegga, Norwegian Sea, Marine Geology 228, pp.15–23.

924 Hudson, J. D. (1977). Stable isotopes and limestone lithification. Journal of the Geological Society,
925 133(6), 637-660.

926 Hustoft, S., Dugan, B., & Mienert, J. (2009). Effects of rapid sedimentation on developing the Nyegga
927 pockmark field: Constraints from hydrological modeling and 3-D seismic data, offshore mid-Norway.
928 Geochemistry, Geophysics, Geosystems, 10(6).

929 Ivanov, M. V., Lein, A. Y., Reeburgh, M. S., Skyring, G.W. (1989). Interaction of sulphur and carbon
930 cycles in marine sediments. Evolution of the Global Biogeochemical Sulphur Cycle. Wiley, Chichester,
931 125-79.

932 Jatiault, R., Dhont, D., Loncke, L., Dubucq, D. (2017). Monitoring of natural oil seepage in the Lower
933 Congo Basin using SAR observations. Remote Sensing of Environment, 191, 258 - 272.
934 http://dx.doi.org/10.1016/j.rse.2017.01.031.

935 Jatiault, R., Dhont, D., Loncke, L., de Madron, X. D., Dubucq, D., Channelliere, C., & Bourrin, F. (2018).
936 Deflection of natural oil droplets through the water column in deep-water environments: The case of
937 the Lower Congo Basin. Deep Sea Research Part I: Oceanographic Research Papers, 136, 44-61.

938 Jatiault, R., Loncke, L., Dhont, D., Imbert, P., Dubucq, D. (2019). Geophysical characterisation of active
939 thermogenic oil seeps in the salt province of the lower Congo basin part I: Detailed study of one oil-
940 seeping site, Marine and Petroleum Geology, doi: https:// doi.org/10.1016/j.marpetgeo.2018.11.026.

941 Jauer, C. D., & Budkewitsch, P. (2010). Old marine seismic and new satellite radar data: Petroleum
942 exploration of north west Labrador Sea, Canada. Marine and Petroleum Geology, 27(7), 1379-1394.
943 doi:10.1016/j.marpetgeo.2010.03.003.

944 Jones, D. M., Head, I. M., Gray, N. D., Adams, J. J., Rowan, A. K., Aitken, C. M., Oldenburg, T. (2008).
945 Crude-oil biodegradation via methanogenesis in subsurface petroleum reservoirs. Nature, 451(7175),
946 176-180.

947 Jones, D.O.B. Walls, A., Clare, M., Fiske, M.S.,Weiland, R.J., O'Brien, R., Touzel, D.F. (2014). Asphalt
948 mounds and associated biota on the Angolan margin, *Deep-Sea Research I*,
949 http://dx.doi.org/10.1016/j.dsr.2014.08.010.

950 Judd, A., & Hovland, M. (2007). Seabed fluid flow: the impact on geology, biology and the marine
951 environment. Cambridge University Press.

952 Karstens, J., & Berndt, C. (2015). Seismic chimneys in the Southern Viking Graben–Implications for
953 palaeo fluid migration and overpressure evolution. *Earth and Planetary Science Letters*, *412*, 88-100.

954 Keller, E. A., Duffy, M., Kennett, J. P., & Hill, T. (2007). Tectonic geomorphology and hydrocarbon
955 induced topography of the mid-channel Anticline, Santa Barbara Basin,
956 California. *Geomorphology*, *89*(3), 274-286.

957 King, L.H., & MacLean, B. (1970). Pockmark on the Scotian Shelf, *Geological Society of America*
958 *Bulletin*, V.81, P.3141-3148.

959 Knittel, K., & Boetius, A. (2009). Anaerobic oxidation of methane: progress with an unknown
960 process. Annual review of microbiology, 63, 311-334.

961 Kornacki, A.S., Kendrick, J.W., Berry, J.L. (1994). Impact of oil and gas vents and slicks on petroleum
962 exploration in the deepwater Gulf of Mexico, *Geo-Marine Letters, 14*, 160-169.

963 Larter, S., Wilhelms, A., Head, I., Koopmans, M., Aplin, A., Di Primio, R., Telnaes, N. (2003). The controls
964 on the composition of biodegraded oils in the deep subsurface—part 1: biodegradation rates in
965 petroleum reservoirs. Organic Geochemistry, 34(4), 601-613.

966 Larter, S., Huang, H., Adams, J., Bennett, B., Jokanola, O., Oldenburg, T., Fowler, M. (2006). The controls
967 on the composition of biodegraded oils in the deep subsurface: Part II—Geological controls on

968 subsurface biodegradation fluxes and constraints on reservoir-fluid property prediction1. AAPG
969 bulletin, 90(6), 921-938.

970 Loncke, L., Mascle, J., Fanil Scientific Parties (2004). Mud volcanoes, gas chimneys, pockmarks and
971 mounds in the Nile deep-sea fan (Eastern Mediterranean): geophysical evidences. Marine and
972 Petroleum Geology, 21, pp 669 – 689, doi:10.1016/j.marpetgeo.2004.02.004.

973 Løseth, H., Gading, M., & Wensaas, L. (2009). Hydrocarbon leakage interpreted on seismic data. Marine
974 and Petroleum Geology, 26(7), 1304-1319.

975 Løseth, H., Wensaas, L., Arntsen, B., Hanken, N., Basire, C., & Graue, K. (2001). 1000 m long gas blow-
976 out pipes. In 63rd EAGE Conference & Exhibition.

977 Løseth, H., Wensaas, L., Arntsen, B., Hanken, N. M., Basire, C., & Graue, K. (2011). 1000 m long gas
978 blow-out pipes. *Marine and Petroleum Geology*, *28*(5), 1047-1060.

979 Lucazeau, F., Brigaud, F., Bouroullec, J-L. (2004). High-resolution heat flow density in the lower Congo
980 basin, *Geochemistry, Geophysics, Geosystems, 5*, http://dx.doi.org/10.1029/2003GC000644.

981 MacDonald, I. R., Bohrmann, G., Escobar, E., Abegg, F., Blanchon, P., Blinova, V., ... & Heeschen, K.
982 (2004). Asphalt volcanism and chemosynthetic life in the Campeche Knolls, Gulf of Mexico. Science,
983 304(5673), 999-1002.

984 MacDonald, I.R., Garcia-Pineda, O., Beet, A., Daneshgar Asl, S., Feng, L., Graettinger, G., French-
985 McCay, D., Holmes, J., Hu, C., Huffer, F., Leifer, I., Muller-Karger, F., Solow, A., Silva, M., Swayze,
986 G. (2015). Natural and unnatural oil slicks in the Gulf of Mexico. *Journal of Geophysical Research:*
987 *Oceans, 120(12)*, 8364-8380.

988 McHargue, T.R. (1990). Stratigraphic Development of Proto-South Atlantic Rifting in Cabinda, Angola –
989 A Petroliferous Lake Basin. In Katz, B.J. (Ed.) Lacustrine Basin Exploration Case Studies and Modern
990 Analogs, 50. AAPG Memoir, p.307-326.

991 MacKay, M. E., Jarrard, R. D., Westbrook, G. K., & Hyndman, R. D. (1994). Origin of bottom-simulating
992 reflectors: geophysical evidence from the Cascadia accretionary prism. Geology, 22(5), 459-462.

993 Maia, A. R., Cartwright, J., & Andersen, E. (2016). Shallow plumbing systems inferred from spatial
994 analysis of pockmark arrays. *Marine and Petroleum Geology*, *77*, 865-881.

995 Marcano, G., Anka, Z., di Primio, R., (2013). Major controlling factors on hydrocarbon generation and
996 leakage in South Atlantic conjugate margins: A comparative study of Colorado, Orange, Campos and
997 Lower Congo basins, Tectonophysics 604, p 17-190.

998 Marcon, Y., Ondréas, H., Sahling, H., Bohrmann, G., & Olu, K. (2014). Fluid flod regimes and growth of
999 a giant pockmark, Geology, Vol.42, Issue 1, pp.63 – 66. http://dx.doi.org/10.1130/G34801.1.

1000 Marton, G.L., Tari, G. C., Lehmann, C. T. (2000). Evolution of the Angolan Passive Margin, West Africa,
1001 With Emphasis on Post-Salt Structural Styles. *Atlantic rifts and continental margins*, 129-149.

1002 Mityagina, M., Lavrova, O., & Bocharova, T. (2007). Detection and discrimination of sea surface films
1003 in the coastal zone of northeastern Black Sea using SAR data. *ESA-ed*, *1*.

1004 Moss, J. L., & Cartwright, J. (2010). 3D seismic expression of km scale fluid escape pipes from offshore
1005 Namibia. Basin Research, 22(4), 481-501.

1006 Mullineaux, L. S., Fisher, C. R., Peterson, C. H., & Schaeffer, S. W. (2000). Tubeworm succession at
1007 hydrothermal vents: use of biogenic cues to reduce habitat selection error?. *Oecologia*, *123*(2), 275-
1008 284.

1009 Nyblade, A. A., & Robinson, S. W. (1994). The african superswell. Geophysical research letters, 21(9),
1010 765-768.

1011 O'Brien, G. W., Lawrence, G. M., Williams, A. K., Glenn, K., Barrett, A. G., Lech, M., Summons, R. E.
1012 (2005). Yampi Shelf, Browse Basin, North-West Shelf, Australia: a test-bed for constraining
1013 hydrocarbon migration and seepage rates using combinations of 2D and 3D seismic data and multiple,

1014 independent remote sensing technologies. Marine and Petroleum Geology, 22(4), 517-549.
1015 doi:10.1016/j.marpetgeo.2004.10.027.

1016 Ondreas, H., Olu, K., Fouquet, Y., Charlou, J.L., Gay, A., Dennielou, B., Donval, J.P., Fifis, A., Nadalig, T.,
1017 Cochonat, P., Cauquil, E., Bourillet, J.F., Le Moigne, M., Sibuet, M. (2005). ROV study of a giant
1018 pockmark on the Gabon continental margin, *Geo-Marine Letters, 25,* 281-292,
1019 http://dx.doi.org/10.1007/s00367-005-0213-6.

1020 Oluboyo, A.P., Gawthorpe, R.L., Bakke, K., Hadler-Jacobsen, F. (2014). Salt tectonic controls on deep-
1021 water turbidite depositional systems: Miocene, southwestern Lower Congo Basin, offshore Angola,
1022 Basin Research 26, 597–620, doi: 10.1111/bre.12051.

1023 Paull, C. K., & Ussler III, W. (2008). Re-evaluating the significance of seafloor accumulations of
1024 methane-derived carbonates: seepage or erosion indicators?.

1025 Peters, K. E., Walters, C. C., & Moldowan, J. M. (2005). The biomarker guide (Vol. 1). Cambridge
1026 University Press.

1027 Peters, K.E., Walters, C.C., Moldowan, J.M. (2007). The Biomarker Guide Volume 2, Biomarkers and
1028 Isotopes in Petroleum Systems and Earth History.

1029 Pierre, C., & Fouquet, Y. (2007). Authigenic carbonates from methane seeps of the Congo deep-sea
1030 fan. *Geo-Marine Letters*, *27*(2-4), 249-257.

1031 Popescu, I., Lericolais, G., Panin, N., De Batist, M., & Gillet, H. (2007). Seismic expression of gas and gas
1032 hydrates across the western Black Sea. Geo-Marine Letters, 27(2-4), 173-183.

1033 Posewang, J., & Mienert, J. (1999). The enigma of double BSRs: indicators for changes in the hydrate
1034 stability field?. Geo-Marine Letters, 19(1-2), 157-163.

1035 Prince, R. C., Lessard, R. R., & Clark, J. R. (2003). Bioremediation of marine oil spills. Oil & Gas Science
1036 and Technology, 58(4), 463-468.

1037 Quirk, D. G., & Pilcher, R. S. (2012). Flip-flop salt tectonics. *Geological Society, London, Special*
1038 *Publications*, *363*(1), 245-264.

1039 Riboulot, V., Sultan, N., Imbert, P., & Ker, S. (2016). Initiation of gas-hydrate pockmark in deep-water
1040 Nigeria: Geo-mechanical analysis and modelling. *Earth and Planetary Science Letters*, *434*, 252-263.

1041 Römer, M., Sahling, H., Pape, T., dos Santos Ferreira, C., Wenzhöfer, F., Boetius, A., & Bohrmann, G.
1042 (2014). Methane fluxes and carbonate deposits at a cold seep area of the Central Nile Deep Sea Fan,
1043 Eastern Mediterranean Sea. Marine Geology, 347, 27-42.
1044 http://dx.doi.org/10.1016/j.margeo.2013.10.011.

1045 Ryan, J. P., Fischer, A. M., Kudela, R. M., McManus, M. A., Myers, J. S., Paduan, J. D., ... & Zhang, Y.
1046 (2010). Recurrent frontal slicks of a coastal ocean upwelling shadow. *Journal of Geophysical Research:*
1047 *Oceans*, *115*(C12).

1048 Sager, W. W., MacDonald, I. R., & Hou, R. (2003). Geophysical signatures of mud mounds at
1049 hydrocarbon seeps on the Louisiana continental slope, northern Gulf of Mexico. *Marine*
1050 *Geology*, *198*(1), 97-132.

1051 Sahling, H., Bohrmann, G., Spiess, V., Bialas, J., Breitzke, M., Ivaniov, I., Kasten, S., Krastel, S., Schneider,
1052 R. (2008). Pockmarks in the Northern Congo Fan area, SW Africa: Complex seafloor features shaped by
1053 fluid flow, *Marine Geology, 249*, 206-225, http://dx.doi.org/10.1016/j.margeo.2007.11.010.

1054 Savoye, B., Cochonat, P., Apprioual, R., Bain, O., Baltzer, A., Bellec, V., ... & Crusson, A. (2000). Structure
1055 et évolution récente de l'éventail turbiditique du Zaïre: premiers résultats scientifiques des missions
1056 d'exploration Zaïango1 & 2 (marge Congo–Angola). Comptes Rendus de l'Académie des Sciences-Series
1057 IIA-Earth and Planetary Science, 331(3), 211-220.

1058 Schoellkopf, N. B., Patterson, B.A. (2000). Petroleum systems of offshore, Cabinda, Angola, in M. R.
1059 Mello and B. J. Katz, Petroleum systems of South Atlantic margins: *AAPG Memoir 73*, 361–376.

1060 Schroot, B. M., & Schüttenhelm, R. T. (2003). Shallow gas and gas seepage: expressions on seismic and
1061 otheracoustic data from the Netherlands North Sea. Journal of Geochemical Exploration, 78, 305-309.

1062 Séranne, M., & Anka, Z. (2005). South Atlantic continental margins of Africa: a comparison of the
1063 tectonic vs climate interplay on the evolution of equatorial west Africa and SW Africa margins. Journal
1064 of African Earth Sciences, 43(1), 283-300.

1065 Séranne M., Séguret M. & Fauchier M. (1992). - Seismic super-units and post-rift evolution of the
1066 continental passive margin of southern Gabon. - Bulletin de la Société Géologique de France, 163, 2,
1067 135 - 146.

1068 Séranne M. (1999). - Early Oligocene stratigraphic turnover on the West Africa continental margin: a
1069 signature of the Tertiary greenhouse-to-icehouse transition? - Terra Nova, 11, 135 - 140.

1070 Serié, C., Huuse, M., & Schødt, N. H. (2012). Gas hydrate pingoes: Deep seafloor evidence of focused
1071 fluid flow on continental margins. *Geology*, *40*(3), 207-210.

1072 Serié, C., Huuse, M., Schødt, N. H., Brooks, J. M., & Williams, A. (2017). Subsurface fluid flow in the
1073 deep-water Kwanza Basin, offshore Angola. Basin Research.

1074 Shanks, W. C. (1995). Mid-Ocean Ridges-Rebirth of a Sea-Floor Vent. *Nature*, *375*(6526), 18-19.

1075 Shank, T. M., Fornari, D. J., Von Damm, K. L., Lilley, M. D., Haymon, R. M., & Lutz, R. A. (1998). Temporal
1076 and spatial patterns of biological community development at nascent deep-sea hydrothermal vents (9
1077 50′ N, East Pacific Rise). *Deep Sea Research Part II: Topical Studies in Oceanography*, *45*(1), 465-515.

1078 Shipley, T. H., Houston, H. H., & Buffler, R. T. (1979). Widespread Occurrence Of Possible Gas-Hydrate
1079 Horizons From Continental Slopes As Identified On Seismic Reflection Profiles. In Offshore Technology
1080 Conference. Offshore Technology Conference.

1081 Sloan, E. D. (1990). Clathrate Hydrates of Natural Gases, 1st ed., 641 pp., Marcel Dekker, New York.

1082 Smrzka, D., Zwicker, J., Klügel, A., Monien, P., Bach, W., Bohrmann, G., & Peckmann, J. (2016).
1083 Establishing criteria to distinguish oil-seep from methane-seep carbonates. Geology, 44(8), 667-670.

1084 Stalvies, C., Talukder, A., Ross, A., Grosjean, E., Carr, A., Williams, A.,... & Jablonski, D. (2017).
1085 Establishing hydrocarbon charge to the Ashmore Platform, Bonaparte Basin, Australia: A natural seeps
1086 study. Marine and Petroleum Geology, 82, 56-68.

1087 Taylor, M. H., Dillon, W. P., & Pecher, I. A. (2000). Trapping and migration of methane associated with
1088 the gas hydrate stability zone at the Blake Ridge Diapir: new insights from seismic data. Marine
1089 Geology, 164(1), 79-89.

1090 Teisserenc, P., & Villemin, J. (1989). Sedimentary basin of Gabon--geology and oil systems.

1091 Thomas, S., Hill, A. J., Clare, M. A., Shreeve, J. W., & Unterseh, S. (2011). Understanding Engineering
1092 Challenges Posed by Natural Hydrocarbon Infiltration and the Development of Authigenic Carbonate.
1093 In *Offshore Technology Conference*. Offshore Technology Conference.

1094 Thrasher, J., Fleet, A.J., Hay, S., Hovland, M. and Düppenbecker, S. (1996). Understanding geology as
1095 the key to using seepage in exploration: The spectrum of seepage styles. In: Schumacher, D. and
1096 Abrams, M.A. (eds.), Hydrocarbon migration and its near-surface expression. American Association of
1097 Petroleum Geologists, Memoir 66, 223-241.

1098 Uenzelmann-Neben, G. (1998). Neogene sedimentation history of the Congo Fan. Marine and
1099 Petroleum Geology, 15(7), 635-650.

1100 Unterseh, S., (2013). Early Recognition of Seabed and Sub-Seabed Natural Hydrocarbon Seeps in Deep
1101 Offshore Angola. 2013 Offshore Technology Conference, May 06 - 09, 2013, Houston, TX, USA.

1102 Valentine, D. L., Reddy, C. M., Farwell, C., Hill, T. M., Pizarro, O., Yoerger, D. R., ... & Clarke, B. A. (2010).
1103 Asphalt volcanoes as a potential source of methane to late Pleistocene coastal waters. *Nature*
1104 *Geoscience*, *3*(5), 345-348.

1105 Wenau, S., Spiess, V., Pape, T., fekete, N. (2014). Cold seeps at the salt front in the Lower Congo Basin
1106 II: The impact of spatial and temporal evolution of salt-tectonics on hydrocarbon seepage, Marine and
1107 Petroleum Geology pp.1 – 14, http://dx.doi.org/10.1016/j.marpetgeo.2014.09.021

1108 Wilkes, H., Rabus, R., Fischer, T., Armstroff, A., Behrends, A., & Widdel, F. (2002). Anaerobic
1109 degradation of n-hexane in a denitrifying bacterium: further degradation of the initial
1110 intermediate (1-methylpentyl) succinate via C-skeleton rearrangement. Archives of Microbiology,
1111 177(3), 235-243.

1112 Williams, A. & Lawrence, G. (2002). The Role of Satellite Seep Detection in exploring the South
1113 Atlantic's Ultradeep Water, in Surface exploration case histories: Applications of geochemistry,
1114 magnetic, and remote sensing, , Shumacher, D., & LeSchack, L.A., eds., *AAPG Studies in geology*
1115 *No. 48 and SEG Geophysical References Series No. 11*, 327-344.

1116 Zander, T., Haeckel, M., Berndt, C., Chi, W. C., Klaucke, I., Bialas, J., ... & Atgın, O. (2017). On the origin
1117 of multiple BSRs in the Danube deep-sea fan, Black Sea. *Earth and Planetary Science Letters*, *462*, 15-
1118 25.

1119 Zengler, K., Richnow, H. H., Rosselló-Mora, R., Michaelis, W., & Widdel, F. (1999). Methane formation
1120 from long-chain alkanes by anaerobic microorganisms. Nature, 401(6750), 266-269.

1121